

August 2020

# **Mesoscale modeling to inform Bison models of accident tolerant fuel concepts**

*Larry Aagesen  
David Andersson  
Benjamin Beeler  
Michael Cooper  
Kyle Gamble  
Yinbin Miao  
Giovanni Pastore  
Michael Tonks  
Pierre-Clement Simon  
Jacob Hirschhorn*



#### NOTICE

This information was prepared as an account of work sponsored by an agency of the U.S. Government. Neither the U.S. Government nor any agency thereof, nor any of their employees, makes any warranty, express or implied, or assumes any legal liability or responsibility for any third party's use, or the results of such use, of any information, apparatus, product, or process disclosed herein, or represents that its use by such third party would not infringe privately owned rights. The views expressed herein are not necessarily those of the U.S. Nuclear Regulatory Commission.

# **Mesoscale modeling to inform Bison models of accident tolerant fuel concepts**

***Larry Aagesen***  
***David Andersson\****  
***Benjamin Beeler***  
***Michael Cooper\****  
***Kyle Gamble***  
***Yinbin Miao\*\****  
***Giovanni Pastore***  
***Michael Tonks\*\*\****  
***Pierre-Clement Simon\*\*\*\****  
***Jacob Hirschhorn\*\*\****

**August 2020**

**Idaho National Laboratory  
Computational Mechanics and Materials Department  
Idaho Falls, Idaho 83415**

**\*Los Alamos National Laboratory  
Materials Science and Technology Division  
Los Alamos, NM 87545**

**\*\*Argonne National Laboratory  
Lemont, IL 60439**

**\*\*\*Department of Materials Science and Engineering  
University of Florida  
Gainesville, FL 32611**

**\*\*\*\*Department of Nuclear Engineering  
The Pennsylvania State University  
University Park, PA 16802**

**Prepared for the  
U.S. Department of Energy  
Office of Nuclear Energy  
Under U.S. Department of Energy-Idaho Operations Office  
Contract DE-AC07-99ID13727**

# ABSTRACT

$\text{U}_3\text{Si}_2$  and doped  $\text{UO}_2$  have been under investigation in recent years as potential accident-tolerant fuel concepts. In this report, lower-length scale studies of these fuel concepts carried out during Fiscal Year 2020 are detailed.

$\text{U}_3\text{Si}_2$  is a potential accident-tolerant fuel that shows promise due to its high thermal conductivity and higher uranium density relative to  $\text{UO}_2$ . However, its swelling and fission gas release behavior in light water reactor (LWR) conditions is relatively unknown. To provide mechanistic insight and determine parameters for engineering-scale fuel performance modeling of pellet-form  $\text{U}_3\text{Si}_2$ , phase-field simulations of the growth, interconnection, and venting of intergranular fission gas bubbles were performed. The fractional coverage of the grain boundary and the fraction of bubble area that is vented were calculated as a function of time. From the simulation data, the fractional grain boundary coverage at saturation, an important parameter needed in engineering-scale modeling of swelling and fission gas release, was determined. Multiple simulations were run to determine the uncertainty in the calculated value. The effect of model assumptions and input parameters that are not well known was evaluated. Simulation results are compared to related theoretical and computational work. Based on the simulation results, a value of 0.60 for the fractional grain boundary coverage at saturation is recommended for  $\text{U}_3\text{Si}_2$  fuel.

Chromium-doped  $\text{UO}_2$  is a widely-studied near-term deployable accident-tolerant fuel concept because it results in a dense, large-grain structure that increases the fuel resistance to densification, swelling, and fission gas release. Densification occurs during reactor operation as pores remaining in the fuel from manufacturing shrink and are gradually eliminated. However, grain growth also occurs concurrently with densification and the resulting grain size change affects the densification process. Thus, it is necessary to have a mechanistic, quantitatively accurate model for grain growth as a basis for a densification model. In this report, the development a mechanistic model of grain growth in undoped  $\text{UO}_2$  fuel during reactor operation. The model development builds on published experimental data on  $\text{UO}_2$  grain growth, as well as atomistic and mesoscale simulation results. We begin by developing new fits with temperature  $T$  (in K) for the average grain boundary (GB) energy and mobility in  $\text{UO}_2$  using literature data, where the GB energy  $\bar{\gamma} = (1.56 - 5.87 \times 10^{-4}T) \pm 0.3 \text{ J/m}^2$  and the GB mobility  $\bar{M} = (2.14 \pm 0.15 \times 10^{-7}) \exp(-(290 \pm 22 \text{ kJ/mol})/RT) \text{ m}^4/(\text{Js})$ . We then discuss the pinning of grain boundaries by porosity, including porosity left over after sintering and fission gas bubbles that form during operation. We present our mechanistic model and validate it using existing grain growth data. Finally, we implement the model in the BISON fuel performance code and quantify its impact for constant and transient power cases. Our model produces similar results to an empirical model for the constant power case, but it predicts more grain growth than the empirical model for the transient power case. We attribute this discrepancy to the new mechanistic model's ability to account for the impact of the temperature and power history. Building on this grain growth model, a coupled model for grain growth and densification in doped  $\text{UO}_2$  will be developed.

# CONTENTS

<b>FIGURES</b>		<b>vi</b>
<b>TABLES</b>		<b>viii</b>
<b>1 Phase-field simulations of intergranular fission gas bubble behavior in <math>\text{U}_3\text{Si}_2</math> nuclear fuel</b>		<b>1</b>
1.1 Introduction . . . . .		1
1.2 Model formulation and parametrization . . . . .		2
1.2.1 Grand potential functional . . . . .		3
1.2.2 Chemical energy contribution and parameterization . . . . .		4
1.2.3 Interfacial energy and parameterization . . . . .		5
1.2.4 Evolution equations . . . . .		6
1.3 Phase-Field Simulations . . . . .		9
1.3.1 Simulation initial conditions . . . . .		9
1.3.2 Simulation results . . . . .		10
1.3.3 Determination of engineering-scale model parameters from simulation results		10
1.3.4 Effect of simulation assumptions and parameters on calculated $F_{c,sat}$ . . . . .		12
1.3.5 Comparison with past theoretical and computational results . . . . .		17
1.4 Conclusions . . . . .		17
<b>2 Mechanistic Grain Growth Model for Fresh and Irradiated <math>\text{UO}_2</math> Nuclear Fuel</b>		<b>19</b>
2.1 Introduction . . . . .		19
2.2 Grain Growth Theory . . . . .		20
2.3 Average GB Energy and Mobility in $\text{UO}_2$ . . . . .		22
2.3.1 Grain boundary energy . . . . .		22
2.3.2 Grain boundary mobility . . . . .		23
2.4 Grain Growth Model with Porosity . . . . .		25
2.4.1 Model of the Resistive Force . . . . .		26
2.4.2 Model of Pore Mobility . . . . .		27
2.4.3 Model of Grain Growth with Mobile Pores . . . . .		29
2.4.4 Grain Growth Model for $\text{UO}_2$ . . . . .		33
2.5 Model Validation . . . . .		34
2.5.1 Grain growth in unirradiated $\text{UO}_2$ . . . . .		34
2.5.2 Grain growth in irradiated $\text{UO}_2$ . . . . .		35
2.6 Impact on Fuel Performance Simulations . . . . .		37
2.7 Conclusions and Future Work . . . . .		40
<b>3 References</b>		<b>42</b>

## FIGURES

1	Evolution of microstructure during simulated growth of grain boundary bubbles in $\text{U}_3\text{Si}_2$ . The grain boundary is shown in blue and the gas bubbles are shown in green. Simulation temperature $T = 1035$ K, $\theta/2 = 73^\circ$ , $n_a = 15/\mu\text{m}^2$ , $l_{\min} = 160$ nm. At $t = 1.97 \times 10^8$ s, all bubbles have connected to the edge of the simulation domain. . . . .	11
2	(a) Fractional grain boundary coverage, $X_{GB}^C$ , and fraction of grain boundary bubbles that are vented, $X_{GB}^V$ , versus time, for the simulation shown in Figure 1. (b) Areal density of grain boundary bubbles, $n_a$ , plotted versus time. (c) Plot of fraction of grain boundary bubbles that are vented, $X_{GB}^V$ , as a function of fractional coverage of the grain boundary by bubbles, $X_{GB}^C$ . . . . .	12
3	Effect of varying $l_{\min}$ on grain boundary saturation behavior. For a smaller $l_{\min} = 130$ nm, $F_{c,sat}$ is delayed to 0.65. For a larger $l_{\min} = 200$ nm, in the earlier stages of venting ( $X_{GB}^C < 0.5$ ) venting is delayed compared to the smaller $l_{\min}$ cases, but the rate of increase is more rapid in the range $0.5 < X_{GB}^C < 0.6$ . . . . .	14
4	(a) Gas bubble microstructure of circular grain boundary with same simulation parameters as those shown in Fig. 1c, at approximately the same time. (b) Comparison of $X_{GB}^V$ versus $X_{GB}^C$ for the square and circular grain boundary geometries. The similarity of the results indicates that the grain boundary geometry does not strongly affect the progress toward venting of the gas bubbles. . . . .	15
5	Effect of defect diffusivity on microstructure. Microstructures are shown at time $t = 1.97 \times 10^8$ s. (a) $D_v = D_g = 0.05$ nm <sup>2</sup> /s, (b) $D_v = D_g = 0.1$ nm <sup>2</sup> /s, (c) $D_v = D_g = 0.5$ nm <sup>2</sup> /s. . . . .	16
6	GB energy values for $\text{UO}_2$ from measurements in the 1970s [1, 2, 3, 4] and more recent MD simulations [5, 6]. Note that the values shown from Ref. [6] are representative values from the hundreds of energies calculated. We also show a linear fit with temperature as a solid black line that we recommend as a reasonable value for the average $\text{UO}_2$ GB energy. The dashed lines show the uncertainty limits of the fit. . . . .	22
7	Our fit of the average $\text{UO}_2$ GB mobility using data from Ainscough et al. [7]. The fit (solid black line) was determined from mobility values converted from rate constants for the four batches with values from three temperatures (labeled “Fit data”). The uncertainty limits (dashed black lines) were determined using data from the other eight batches (labeled “Error bar data”). Data from other researchers taken from Tab. 11 in Ref. [7] are shown for comparison. Data from Yao et al. [8] and the corresponding mobility fits are also shown. . . . .	24
8	Demonstration of the impact of a pore size distribution. (a) demonstrates that it is not possible to guarantee radii above zero when using a normal distribution by showing the probability density function (PDF) for a pore radius that follows a uniform, lognormal, and normal distribution. (b) compares the expected value of the inverse of the pore radius versus the ratio of the pore radius standard deviation to the mean from uniform and lognormal distributions. Both plots were made assuming an average pore radius $\bar{r}_p = 5$ nm . . . . .	27
9	The expected value $E(r_p^{-4})$ versus the ratio of the pore radius standard deviation to the mean for uniform and lognormal distributions, where (a) shows the values for the $\bar{r}_p = 1$ $\mu\text{m}$ value used in the fit and (b) shows the values for $\bar{r}_p = 5$ nm. Note that the fit is accurate for both average radii. . . . .	29

10	The velocity of a $\text{UO}_2$ GB with a radius of curvature $R_g = 7 \mu\text{m}$ predicted by our new model (Eq. (65)) for various pore radii. (a) and (b) compare the value from the new model with that predicted by the $M_{eff}$ (Eq. (62)) and the pinning model with static particles (Eq. (33)). The different regimes are shaded and labeled, where light green indicates Regime 1, light purple indicates Regime 2, light orange indicates Regime 3, and light blue indicates Regime 4. (c) and (d) demonstrate the impact of a lognormal pore size distribution, where the line colors indicate the ratio of the pore radius standard deviation to its mean. The cases shown in (a) and (c) have $f_c = 0.05$ and the values of $N_p$ changing with pore radius. The cases shown in (b) and (d) have $N_p = 2.5 \times 10^{10}$ pores/ $\text{m}^2$ and the value of $f_c$ changing with radius. . . . .	31
11	Validation of our new grain growth model by comparing to grain growth data for unirradiated $\text{UO}_2$ [7]. Specifically, we compare against data from Batches 3, 7, and 12. The average pore radii were fit using the data at $1400^\circ\text{C}$ , shown in (a), and we validated the model using the data at $1500^\circ\text{C}$ , shown in (b). . . . .	35
12	Comparison of the grain sizes from our grain growth model to those predicted by the empirical model using values taken from BISON simulations. Results using a linear power of $29 \text{ kW/m}$ are on the left and using a linear power of $37 \text{ kW/m}$ are on the right. (a) shows the results using the published surface diffusion activation energy, and (b) shows the results using the activation energy that was calibrated using the $29 \text{ kW/m}$ result. In each figure, solid lines show results from our new model, and dashed lines show results from the empirical model [7]. . . . .	37
13	Impact of our grain growth model on fuel performance simulations using BISON for constant and transient power cases. (a) and (b) show the average linear heat rates for the two cases. (c) - (f) show results for the constant power case, and (g) - (j) show results for the transient power case. (c) and (g) show the pellet temperature with time at three radial locations at an axial location of $2 \text{ m}$ (approximately mid-rod), (d) and (h) show the grain size with time at the same radial and axial locations, (e) and (i) show the fractional fission gas release with time, and (f) and (j) show the gaseous swelling at the same locations. In each figure, solid lines show results obtained using the new grain growth model and dashed lines show results obtained using the empirical model from Ainscough et al. [7]. . . . .	39

## TABLES

1	Parameters used for phase-field simulations. . . . .	9
2	Variation in calculated engineering-scale model parameter $F_{c,sat}$ for varying initial grain boundary bubble positions. For this set of simulations, the parameters used are the same as those for the simulations shown in Fig. 1, and only the random positions of the bubbles in the initial conditions are varied. . . . .	13
3	Properties for $\text{UO}_2$ needed to calculate the pore mobility. The value or expression for each property is provided, as well as the reference when applicable. . . . .	31



# 1 Phase-field simulations of intergranular fission gas bubble behavior in $\text{U}_3\text{Si}_2$ nuclear fuel

## 1.1 Introduction

In recent years, the desire for commercial nuclear reactor fuels that are more tolerant of accident conditions has driven research into alternatives to the  $\text{UO}_2$  pellets clad in Zircaloy that are currently used in light water reactors (LWRs). One promising candidate for accident-tolerant fuel (ATF) applications is  $\text{U}_3\text{Si}_2$ , due to its higher thermal conductivity compared to  $\text{UO}_2$  [9]. Although  $\text{U}_3\text{Si}_2$ 's melting temperature is lower than that of  $\text{UO}_2$ , its much higher thermal conductivity results in greater margin to the melting temperature in both normal operation and accident conditions [10, 11].

Despite these potential advantages, the swelling behavior of  $\text{U}_3\text{Si}_2$  remains poorly understood. Past experience with dispersion-form  $\text{U}_3\text{Si}_2$  fuel in research reactors [12] has indicated that swelling could be a significant issue in  $\text{U}_3\text{Si}_2$ ; however, it is unknown whether swelling in dispersion fuel in research reactors is representative of swelling that would be encountered in pellet-form fuel at the higher temperatures typical of commercial LWRs. Dispersion-form  $\text{U}_3\text{Si}_2$  undergoes fission-induced amorphization [12], which may strongly influence swelling. However, the much higher operating temperatures of pellet-form fuel in LWRs may prevent fission-induced amorphization [13, 14, 15, 16, 17]; based on experimental observations of ion irradiation,  $\text{U}_3\text{Si}_2$  is crystalline for temperatures of 350 °C and above [13], and simulations with Idaho National Laboratory's fuel performance code BISON show that temperature throughout a  $\text{U}_3\text{Si}_2$  LWR pellet remains above 350 °C throughout fuel lifetime during steady-state operation [11]. Thus, given the expected lack of amorphization in  $\text{U}_3\text{Si}_2$  LWR fuel, the mechanism of swelling may be different from research reactors. The only data extant on pellet-form  $\text{U}_3\text{Si}_2$  indicates that swelling could be greater than 10% for a low burnup of 0.65% fissions per initial metal atom (FIMA) [18].

To provide predictive capability for the performance of  $\text{U}_3\text{Si}_2$  nuclear fuel, several computational modeling approaches have been employed. Rest developed a model for the behavior of  $\text{U}_3\text{Si}_2$  under conditions typical of research reactors, where amorphization of  $\text{U}_3\text{Si}_2$  would be expected to occur [19]. Miao et al. parameterized a rate theory model for fission gas behavior and applied it to study swelling of  $\text{U}_3\text{Si}_2$  in LWRs [10, 11]. Barani et al. recently developed a model for  $\text{U}_3\text{Si}_2$  fission gas behavior in LWRs [20], implemented in BISON. The model tracks the populations of intragranular and intergranular bubbles. It assumes that, similar to  $\text{UO}_2$  fuel, fission gas atoms can be trapped in intragranular bubbles and subsequently re-solved back into the matrix due to impacts by energetic fission fragments. The balance between trapping and re-resolution affects the rate of transport of fission gas atoms to grain boundaries. Also similar to  $\text{UO}_2$ , the model assumes that fission gas release from the fuel is controlled by the grain boundary (intergranular) bubbles. This is based on experimental observations of  $\text{U}_3\text{Si}_2$  irradiated at LWR temperatures [18], which showed the presence of intergranular bubbles with sizes comparable to those observed in  $\text{UO}_2$ . The model tracks the number density and size of the bubbles and calculates the fractional coverage of the grain boundaries until the onset of gas release at the attainment of a saturation coverage value, based on the approach of Ref. [21].

In Ref. [20], a sensitivity analysis was carried out to determine the model parameters that most strongly influence swelling and fission gas release (FGR). Two parameters that had a strong impact on the predictions of these quantities were the surface energy between the fuel matrix and intergranular bubbles,  $\sigma_{mb}$ , and the intergranular bubbles' dihedral angle  $\theta$ , which is determined by the balance of surface energy and grain boundary energy. Improved estimates for these parameters

were recently developed based on [22] as  $\sigma_{mb} = 1.7 \text{ J/m}^2$  and  $\theta = 146^\circ$ . Another parameter that strongly affected swelling and FGR was the saturation coverage of grain boundaries,  $F_{c,sat}$ . In the model, the fractional coverage of the grain boundaries by intergranular bubbles,  $F_c$ , is tracked and increases as the bubbles grow and coalesce until it reaches  $F_{c,sat}$ . At that point, it is assumed that the bubbles interconnect to form a percolated network across the grain boundary, and that a free path exists from interior grain boundaries to free surfaces of the pellet (possibly through a network of tunnels that forms along the triple junctions in the grain structure [23]). Therefore, the model assumes that when  $F_c = F_{c,sat}$  at a particular location, all gas contained in the intergranular bubbles at that location is released to the free space between the fuel and cladding. From that point on,  $F_c$  does not increase past  $F_{c,sat}$ , and any fission gas reaching the grain boundaries at that location is immediately transported to the free space between the fuel and cladding.

Based on experimental observations of intergranular bubbles [24], a value of  $F_{c,sat} = 0.5$  has been used for simulations of swelling and FGR in  $\text{UO}_2$  [21, 25]. However, to our knowledge there is insufficient experimental evidence to determine  $F_{c,sat}$  for  $\text{U}_3\text{Si}_2$  fuel at LWR operating temperatures. For this reason, in Ref. [20], the theoretical value for saturation coverage by a uniform square lattice,  $F_{c,sat} = 0.78$ , was used [26].

In past work, phase-field simulations were used to investigate the process of growth, interconnection, and venting of grain boundary bubbles in  $\text{UO}_2$  [27]. In that work, the phase-field model included the effects of surface and grain boundary energies to capture the bubble morphology correctly. Bubble growth was driven by supersaturation of fission gas atoms in the fuel matrix surrounding the bubbles; thus, the simulation conditions were more representative of post-irradiation annealing than normal operation. Ref. [27] investigated the rate at which the bubbles vented to a triple junction network that was assumed to exist at the periphery of the simulation domain. It was found that two of the most important factors controlling the rate at which bubbles vented were the bubble dihedral angle and the areal density of the bubbles.

In this work, we employ an approach similar to Ref. [27] to investigate the progress toward venting of grain boundary bubbles in  $\text{U}_3\text{Si}_2$ , and use the phase-field simulation results to determine a value for  $F_{c,sat}$  for  $\text{U}_3\text{Si}_2$  to be used in the fission gas release model described in Ref. [20]. We employ a phase-field model implemented within Marmot, Idaho National Laboratory’s mesoscale simulation code [28]. The model in the present work incorporates additional physics beyond the model used in Ref. [27], including tracking of both vacancy and fission gas defect species, dependence of the bulk free energy density on these defect species concentrations, and source terms for the production of these defect species at normal LWR operating conditions. The model was originally presented and parametrized for  $\text{UO}_2$  in Ref. [23]. Here, the model is parametrized for  $\text{U}_3\text{Si}_2$  using atomistic and rate theory simulation results. The remainder of this work is organized as follows. In Section 1.2, the phase-field model formulation and parametrization is described. In Section 1.3, the simulation results are presented and analyzed to determine  $F_{c,sat}$  for  $\text{U}_3\text{Si}_2$ , uncertainties associated with the model and with input parameters that are not well known are determined, and the results are compared with related past theoretical and computational work. Finally, in Section 1.4, conclusions are drawn and directions for future work are suggested.

## 1.2 Model formulation and parametrization

The phase-field model used to simulate the evolution of the intergranular bubbles was originally described in Ref. [23]. Key features of the model and parametrization for  $\text{U}_3\text{Si}_2$  are given in the remainder of this section. The microstructure of the fuel consists of multiple grains of  $\text{U}_3\text{Si}_2$  and intergranular fission gas bubbles. In the phase-field model, the microstructure is represented with a set of order parameters. For a microstructure consisting of  $p$  grains, the individual grains of the

fuel matrix are represented by a set of order parameters  $\eta_{m1}, \eta_{m2}, \dots, \eta_{mp}$ . Each fission gas bubble is crystallographically indistinguishable from the others, so the bubbles are represented by a single order parameter  $\eta_{b0}$ . Within the interior of grain  $i$  of the fuel,  $\eta_{mi} = 1$ ,  $\eta_{mj} = 0 \forall j \neq i$ , and  $\eta_{b0} = 0$ . Within the bubble phase,  $\eta_{b0} = 1$  and  $\eta_{mj} = 0 \forall j$ . Interfaces between grains are represented by a smooth variation of the order parameters.

In addition to the local crystal structure, the local concentration of defect species is also used to describe the microstructure. In the present model, we assume that the dominant defect species are U vacancies and fission gas atoms on U lattice sites. Both U vacancies and interstitials are produced by collision cascades; however, interstitials are much more mobile and therefore diffuse to sinks much more rapidly than vacancies. Therefore, there is a net formation of vacancies which can be represented by a source term for net vacancy production. For fission gas atoms on U lattice sites, the formation of bubbles is driven by the low-solubility Xe and Kr atoms. We assume that the properties of all insoluble fission gas atoms can be described by the properties of Xe atoms on U sites, since Xe production occurs at a rate nearly ten times that of Kr [29]. The density of vacancies and gas atoms are represented by variables  $\rho_v$  and  $\rho_g$ , respectively, with units of number of defects per unit volume. These quantities can be converted to the local composition (mole fraction)  $c$  of the U lattice using  $c = \rho V_a$ , where  $V_a$  is the atomic volume occupied by a U atom in the  $U_3Si_2$  crystal structure.  $V_a$  was calculated to be  $0.0363 \text{ nm}^3$  by dividing the unit cell volume of  $0.218 \text{ nm}^3$  (calculated from experimental data [9]) by 6 U atoms in the unit cell.

### 1.2.1 Grand potential functional

To derive the evolution equations for the microstructure, the total grand potential  $\Omega$  of the system is written as a function of the local grand potential density:

$$\Omega = \int_V \left( m \left[ \sum_{\alpha} \sum_{i=1}^{p_{\alpha}} \left( \frac{\eta_{\alpha i}^4}{4} - \frac{\eta_{\alpha i}^2}{2} \right) + \sum_{\alpha} \sum_{i=1}^{p_{\alpha}} \left( \sum_{\beta} \sum_{j=1, \alpha i \neq \beta j}^{p_{\beta}} \frac{\gamma_{\alpha i \beta j}}{2} \eta_{\alpha i}^2 \eta_{\beta j}^2 \right) + \frac{1}{4} \right] + \frac{\kappa}{2} \sum_{\alpha} \sum_{i=1}^{p_{\alpha}} |\nabla \eta_{\alpha i}|^2 + \sum_{\alpha} h_{\alpha} \omega_{\alpha} \right) dV \quad (1)$$

where  $\alpha$  and  $\beta$  are indices for phases,  $i$  and  $j$  are indices for grains of each phase,  $p_{\alpha}$  and  $p_{\beta}$  are the number of grains of phase  $\alpha$  and  $\beta$ ,  $m$  is a constant free energy barrier coefficient,  $\kappa$  is the gradient energy coefficient (considered to be independent of interface orientation and misinclination here), and the set of constant coefficients  $\gamma_{\alpha i \beta j}$  allow the adjustment of interfacial energies between phases and grains.  $\omega_{\alpha}$  is the local grand potential density of each phase, and  $h_{\alpha}$  is a switching function for phase  $\alpha$  that has value  $h_{\alpha} = 1$  in phase  $\alpha$  and  $h_{\alpha} = 0$  in all other phases. In Eq. (1), the first and second terms ensure that a minimum in the free energy exists within the interior of each grain, and contribute to the interfacial energies between different phases/grains. The third term ( $\frac{m}{4}$ ) is added to make the homogeneous free energy density equal to 0 within grain interiors. The fourth term penalizes gradients in the order parameters representing each grain and also contributes to the interfacial energies between different grains/phases. The fifth term adds the appropriate grand potential density for each phase. The switching function used to interpolate the grand potential densities was introduced in Ref. [30] and has the form

$$h_{\alpha} = \frac{\sum_{i=1}^{p_{\alpha}} \eta_{\alpha i}^2}{\sum_{\beta} \sum_{i=1}^{p_{\beta}} \eta_{\beta i}^2} \quad (2)$$

For the matrix and bubble phases, the switching functions reduce to

$$h_m = \frac{\sum_{i=1}^p \eta_{mi}^2}{\eta_{b0} + \sum_{i=1}^p \eta_{mi}^2} \quad (3)$$

$$h_b = \frac{\eta_{b0}}{\eta_{b0} + \sum_{i=1}^p \eta_{mi}^2} \quad (4)$$

The grand potential density for each phase is given by

$$\omega_m = f_m - \mu_g \rho_g - \mu_v \rho_v \quad (5)$$

$$\omega_b = f_b - \mu_g \rho_g - \mu_v \rho_v \quad (6)$$

where  $f_m$  and  $f_b$  are the Helmholtz free energies of each phase and  $\mu_g$  and  $\mu_v$  are the chemical potentials of the gas atoms and vacancies, respectively. The Helmholtz free energies are given by

$$f_m = f_{m,chem} \quad (7)$$

$$f_b = f_{b,chem} \quad (8)$$

where  $f_{m,chem}$  and  $f_{b,chem}$  are the chemical energy contributions. As in Ref. [23], the bubbles are assumed to have gas pressure at the equilibrium pressure for their size as determined by the Laplace-Young equation; thus, the surface tension of the bubble-matrix interface balances the gas bubble pressure and no stress is exerted by the bubbles on the surrounding fuel matrix. Therefore, no contribution to the Helmholtz free energy due to elastic deformation is included.

## 1.2.2 Chemical energy contribution and parameterization

Using the ideal solution model, the Helmholtz free energy density is written

$$f_{m,ideal} = \frac{1}{V_m} \{ RT[c_v \ln c_v + (1 - c_v) \ln (1 - c_v)] + N_A E_v^f c_v + RT[c_g \ln c_g + (1 - c_g) \ln (1 - c_g)] + N_A E_g^f c_g \} \quad (9)$$

where  $V_m$  is the molar volume,  $R$  is the ideal gas constant,  $V_m = V_a N_A$ ,  $N_A$  is Avogadro's number,  $E_v^f$  is the formation energy of a U vacancy, and  $E_g^f$  is the formation (solution) energy of a gas (Xe) atom on a U lattice site, and  $T$  is the temperature (assumed to be 1035 K, representative of temperature at the fuel centerline during high power LWR conditions). As determined from DFT calculations [31],  $E_v^f = 1.69$  eV and  $E_g^f = 4.92$  eV. To simplify the numerical solution of the governing equations,  $f_{m,ideal}$  was approximated with a parabolic function:

$$f_{m,chem} = \frac{1}{2} k_v^m (c_v - c_v^{m,eq})^2 + \frac{1}{2} k_g^m (c_g - c_g^{m,eq})^2 \quad (10)$$

where  $k_v^m$  and  $k_g^m$  are the curvatures of the parabolas and  $c_v^{m,eq}$  and  $c_g^{m,eq}$  are the equilibrium composition of vacancies and gas atoms in the  $U_3Si_2$  matrix. The equilibrium compositions are determined from the formation energies and temperature using  $c_v^{m,eq} = \exp(-E_v^f/k_B T)$  and  $c_g^{m,eq} = \exp(-E_g^f/k_B T)$ . The curvatures of the parabolas are set by assuming that when the vacancy composition,  $c_v$ , is equal to the steady-state vacancy composition during reactor operation,  $c_v^0$ , the

chemical potential determined from the parabolic approximation is equal to the chemical potential of the ideal solution model, as originally described in Ref. [32]. Since  $\mu = \frac{\partial f}{\partial \rho} = \frac{\partial f}{\partial c} \frac{\partial c}{\partial \rho} = V_a \frac{\partial f}{\partial c}$ ,

$$V_a \frac{\partial f_{m,chem}}{\partial c_v} \Big|_{c_v^0} = V_a \frac{\partial f_{m,ideal}}{\partial c_v} \Big|_{c_v^0} \quad (11)$$

This leads to an expression for  $k_v^m$ , assuming  $c_v^0 = 5 \times 10^{-3}$ :

$$k_v^m = \frac{1}{(c_v^0 - c_v^{m,eq})} \left[ \frac{RT}{V_m} [\ln c_v^0 - \ln (1 - c_v^0)] + \frac{N_A E_v^f}{V_m} \right] = 5.38 \times 10^{11} \text{ J/m}^3 \quad (12)$$

For simplicity, it is assumed that  $k_v^m = k_g^m$ .

The bulk chemical free energy density of the gas bubble phase,  $f_{b,chem}$ , is determined by considering the gas phase to be a mixture of U-site vacancies and Xe atoms as described in Ref. [23]. It is assumed that the van der Waals gas equation of state applies to Xe [29], in which the gas atoms are assumed to have a hard-sphere exclusion volume characterized by the parameter  $b$ , and we neglect long-range interactions due to the high density of gas in the bubbles. For Xe,  $b = 0.085 \text{ nm}^3/\text{atom}$  [29]. With these assumptions, the Helmholtz free energy density of the gas is [33]:

$$f_{b,vdW} = n_g kT \left[ \ln \left( \frac{1}{n_Q \left( \frac{1}{n_g} - b \right)} \right) - 1 \right] + f_0 \quad (13)$$

where  $n_g$  is the number density of gas atoms,  $n_Q = \left( \frac{mk_B T}{2\pi\hbar} \right)^{3/2}$  is the quantum concentration,  $m$  is the mass of a Xe atom, and  $f_0$  is the offset to ensure that the solid and gas free energies are measured relative to the same reference state.  $n_g$  can be put in terms of the model variables using  $n_g = c_g n_U$  (where  $n_U = 1/V_a$  is the number density of U atoms in the  $\text{U}_3\text{Si}_2$  lattice) as long as  $c_v + c_g = 1$  holds.  $f_0$  is determined by setting the minima of the gas and solid phase free energies equal to each other, resulting in  $f_0 = 1.82 \times 10^9 \text{ J/m}^3$ .

To simplify numerical calculations, a parabolic approximation was also fit to the Helmholtz free energy of the gas phase:

$$f_{b,chem} = \frac{1}{2} k_v^b (c_v - c_v^{b,eq})^2 + \frac{1}{2} k_g^b (c_g - c_g^{b,eq})^2 \quad (14)$$

The minimum of the parabolic free energy was set to occur at the minimum of the van der Waals free energy, resulting in  $c_g^{b,eq} = 0.3924$  and  $c_v^{b,eq} = 0.6076$ . Because composition in the gas bubbles will generally not deviate far from the minimum of the free energy,  $k_v^b$  and  $k_g^b$  were set by assuming  $k_v^b = k_g^b$  and fitting to  $f_{b,vdW}$  in the range  $0.36 < c_g < 0.42$ , resulting in  $k_v^b = k_g^b = 8.0 \times 10^{10} \text{ J/m}^3$ .

### 1.2.3 Interfacial energy and parameterization

Based on the results of Ref. [22], the interfacial energy between the matrix and gas bubble phase was calculated to be  $\sigma_{mb} = 1.7 \text{ J/m}^2$ . Although a range of energies was calculated for different grain boundaries in Ref. [22], the current BISON model for fission gas release only considers a single dihedral angle for intergranular bubbles. Therefore, for the purposes of the present work, a single representative grain boundary energy was chosen to be  $\sigma_{mm} = 1.0 \text{ J/m}^2$ . For an intergranular bubble, this results in a dihedral angle of  $146^\circ$ . In this section, the process of choosing phase-field model parameters to accurately include these interfacial and grain boundary energies is described.

Using the grand potential functional of Eq. (1), the interfacial energy  $\sigma_{\alpha i \beta j}$  between grain  $i$  of phase  $\alpha$  and grain  $j$  of phase  $\beta$  is given by [34, 30]

$$\sigma_{\alpha i \beta j} = g(\gamma_{\alpha i \beta j}) \sqrt{\kappa m} \quad (15)$$

where  $g(\gamma_{\alpha i \beta j})$  is a dimensionless function of  $\gamma$  that in general must be evaluated numerically. However, for the special case  $\gamma = 1.5$ ,  $g(\gamma = 1.5) = \sqrt{2}/3$ . For this special case, analytical expressions can be used that relate  $\kappa$  and  $m$  to the interfacial energy and characteristic thickness  $l_{int}$  of the interface [34, 30]:

$$\kappa = \frac{3}{4} \sigma_{mb} l_{int} \quad (16)$$

$$m = \frac{6 \sigma_{mb}}{l_{int}} \quad (17)$$

To resolve the intergranular bubbles,  $l_{int}$  is chosen to be 30 nm, and we choose the interface between any grain  $i$  of the matrix phase and the bubble phase to have  $\gamma_{mib0} = 1.5$ , resulting in  $\kappa = 1.92 \times 10^{-8}$  J/m and  $m = 6.84 \times 10^8$  J/m<sup>3</sup>. To control the grain boundary energies, since  $\kappa$  and  $m$  are fixed, the parameters  $\gamma_{mimj}$  must be determined to obtain the correct value of  $\sigma_{mm}$ , which is assumed to be constant and isotropic for all interfaces between grains  $i$  and  $j$ . To determine the value of  $\gamma_{mimj}$ , using Eq. (15),

$$\sigma_{mb} = g(\gamma_{mib0}) \sqrt{\kappa m} \quad (18)$$

$$\sigma_{mm} = g(\gamma_{mimj}) \sqrt{\kappa m} \quad (19)$$

Dividing Eq. (18) by Eq. (19),

$$\frac{\sigma_{mb}}{\sigma_{mm}} = \frac{g(\gamma_{mib0})}{g(\gamma_{mimj})} \quad (20)$$

Rearranging Eq. (20),

$$g(\gamma_{mimj}) = g(\gamma_{mib0} = 1.5) \frac{\sigma_{mm}}{\sigma_{mb}} = \frac{\sqrt{2}}{3} \frac{1.0}{1.7} = 0.27 \quad (21)$$

A polynomial approximation has been fit to numerical results that allows  $\gamma$  to be found as a function of  $g$  [35]:

$$\gamma = (-5.288g^8 - 0.09364g^6 + 9.965g^4 - 8.813g^2 + 2.007)^{-1} \quad (22)$$

Using this approximation,  $\gamma_{mimj} = 0.67$ .

## 1.2.4 Evolution equations

From the grand potential functional of Eq. (1), the Allen-Cahn equations for evolution of the order parameters can be derived:

$$\begin{aligned} \frac{\partial \eta_{\alpha i}}{\partial t} &= -L \frac{\delta \Omega}{\delta \eta_{\alpha i}} \\ \frac{\partial \eta_{\alpha i}}{\partial t} &= -L \left[ m \left( \eta_{\alpha i}^3 - \eta_{\alpha i} + 2\eta_{\alpha i} \sum_{\beta} \sum_{j=1, \alpha i \neq \beta j}^{p_{\beta}} \gamma_{\alpha i \beta j} \eta_{\beta j}^2 \right) \right. \\ &\quad \left. - \kappa \nabla^2 \eta_{\alpha i} + \sum_{\alpha} \frac{\partial h_{\alpha}}{\partial \eta_{\alpha i}} \omega_{\alpha} \right] \end{aligned} \quad (23)$$

where  $\frac{\delta\Omega}{\delta\eta_{\alpha i}}$  is the variational derivative of  $\Omega$  with respect to order parameter  $\eta_{\alpha i}$  and  $L$  is the order parameter mobility, which in general is a function of order parameters and concentration. Parameterization of  $L$  will be discussed later in this section.

To evolve the gas and vacancy concentrations, it is more convenient to write the evolution equations in terms of chemical potentials  $\mu_v$  and  $\mu_g$  and use the chemical potentials as the field variables rather than densities. To enable this, the grand potentials in each phase, Eq. (5) - (6), must be expressed in terms of  $\mu_v$  and  $\mu_g$ . For the matrix phase, the relation  $\mu_g = V_a \frac{\partial f_{m,chem}}{\partial c_g} = V_a k_g^m (c_g - c_g^{m,eq})$  can be re-arranged to yield

$$c_g = \frac{\mu_g}{V_a k_g^m} + c_g^{m,eq} \quad (24)$$

Similarly,

$$c_v = \frac{\mu_v}{V_a k_v^m} + c_v^{m,eq} \quad (25)$$

Eq. (24) - (25) can be used in conjunction with the relations  $\rho_g = \frac{c_g}{V_a}$ ,  $\rho_v = \frac{c_v}{V_a}$ , Eq. (5), (7), and (10) to obtain the grand potential density as a function of chemical potentials rather than concentrations:

$$\omega_m = -\frac{1}{2} \frac{\mu_v^2}{V_a^2 k_v^m} - \frac{\mu_v}{V_a} c_v^{m,eq} - \frac{1}{2} \frac{\mu_g^2}{V_a^2 k_g^m} - \frac{\mu_g}{V_a} c_g^{m,eq} \quad (26)$$

Similarly, the grand potential density of the bubble phase can be expressed as

$$\omega_b = -\frac{1}{2} \frac{\mu_v^2}{V_a^2 k_v^b} - \frac{\mu_v}{V_a} c_v^{b,eq} - \frac{1}{2} \frac{\mu_g^2}{V_a^2 k_g^b} - \frac{\mu_g}{V_a} c_g^{b,eq} \quad (27)$$

The evolution equations for  $\mu_g$  and  $\mu_v$  are

$$\frac{\partial \mu_g}{\partial t} = \frac{1}{\chi_g} \left[ \nabla \cdot (D_g \chi_g \nabla \mu_g) + s_g - \sum_{\alpha} \sum_{i=1}^{p_{\alpha}} \frac{\partial \rho_g}{\partial \eta_{\alpha i}} \frac{\partial \eta_{\alpha i}}{\partial t} \right] \quad (28)$$

$$\frac{\partial \mu_v}{\partial t} = \frac{1}{\chi_v} \left[ \nabla \cdot (D_v \chi_v \nabla \mu_v) + s_v - \sum_{\alpha} \sum_{i=1}^{p_{\alpha}} \frac{\partial \rho_v}{\partial \eta_{\alpha i}} \frac{\partial \eta_{\alpha i}}{\partial t} \right] \quad (29)$$

where  $\chi_g$  and  $\chi_v$  are the susceptibilities as defined later in this section,  $D_g$  and  $D_v$  are the diffusion coefficients, and  $s_g$  and  $s_v$  are the source terms for production of Xe atoms and U site vacancies.

The source term  $s_g = s_g^0 h_m$  is given by a constant rate of Xe production,  $s_g^0$ , times the switching function  $h_m$ , which has a value of 1 in the fuel matrix and zero inside the bubble. This is to limit production of new Xe atoms to the fuel matrix in the model. The Xe production rate  $s_g^0 = \dot{F} Y_{Xe}$ , where  $\dot{F}$  is the fission rate density and  $Y_{Xe}$  is the fission yield of Xe.  $\dot{F}$  is estimated to be  $1.26 \times 10^{13}$  fissions/(cm<sup>3</sup> s) based on typical operating values for a light water reactor [29], scaled up to account for the increased U site density of U<sub>3</sub>Si<sub>2</sub> compared with UO<sub>2</sub>.  $Y_{Xe}$  is taken to be 0.2156 based on the thermal neutron Xe yield for U-235 [36]. The vacancy production rate is similarly given by  $s_v = s_v^0 h_m$ .  $s_v^0$  has not been determined to our knowledge, so we assume a value of  $s_v^0 = 10 s_g^0$ .

The susceptibility  $\chi$  describes the relationship between solute density and its chemical potential:  $\chi = \frac{\partial \rho}{\partial \mu}$  [37]. This relationship differs based on the phase of the system, so  $\chi$  is interpolated based on the local phase using the switching functions  $h_{\alpha}$ . For gas atoms,

$$\chi_g = h_m \chi_g^m + h_b \chi_g^b \quad (30)$$

where  $\chi_g^m = \frac{\partial \rho_g^m}{\partial \mu_g}$  and  $\chi_g^b = \frac{\partial \rho_g^b}{\partial \mu_g}$ . Since the governing equations are in terms of the chemical potentials, the susceptibilities must also be expressed in terms of chemical potentials, which can be done as follows. Using  $\rho_g^m = \frac{c_g}{V_a}$ , and substituting for  $c_g$  using Eq. (24),  $\chi_g^m = \frac{\partial \rho_g^m}{\partial \mu_g} = \frac{1}{V_a^2 k_g^m}$ . Similar expressions can be derived for  $\chi_v^m$ ,  $\chi_g^b$ , and  $\chi_v^b$ , resulting in

$$\chi_g = h_m \frac{1}{V_a^2 k_g^m} + h_b \frac{1}{V_a^2 k_g^b} \quad (31)$$

$$\chi_v = h_m \frac{1}{V_a^2 k_v^m} + h_b \frac{1}{V_a^2 k_v^b} \quad (32)$$

The diffusivity of Xe atoms was taken from recent atomistic calculations [31, 38]. For stoichiometric  $\text{U}_3\text{Si}_2$ , Xe diffusivity is assumed to be dominated by transport in the  $aa$  direction of the unit cell (as described in Ref. [31]), and diffusivity is given by  $D_g = D_1 + D_3$ .  $D_1$  is the thermal diffusivity and is given by  $D_1 = D_0 \exp \frac{-E_m}{k_B T}$ , where  $D_0 = 2.85 \times 10^{-4} \text{ m}^2/\text{s}$  and  $E_m = 3.17 \text{ eV}$ .  $D_3$  is the athermal diffusivity, a measure of effective diffusion from radiation damage-induced ballistic mixing, and is given by  $D_3 = 3.58 \times 10^{-42} \dot{F}$  [38]. At the simulation temperature of 1035 K, thermal diffusivity dominates, and  $D_g = 0.1 \text{ nm}^2/\text{s}$ . The rate of vacancy transport to fission gas bubbles is influenced by the balance between the rate of vacancy production,  $s_v^0$ , and the diffusion coefficient of vacancies,  $D_v$ . Since  $s_v^0$  is not well known and we are using an assumed value, we further assume that the diffusivity of vacancies is the same as that of gas atoms:  $D_v = D_g$ . The much larger value of  $s_v^0$  ensures that a large supply of vacancies is available and therefore gas bubble growth is limited by the supply of gas atoms, consistent with the typical assumptions of bubble growth during steady-state reactor operating conditions [29].

In order to optimize the performance of the PetSC nonlinear solver used in the numerical solution of the problem for each time step, the governing equations were non-dimensionalized so that all problem quantities are of order unity, using length scale  $l^* = 1 \text{ nm}$ , time scale  $\tau^* = 0.1 \text{ s}$ , and energy density scale  $E^* = 63 \times 10^9 \text{ J/m}^3$ . Finally, we describe the parameterization of the order parameter mobility  $L$ . In the simulation configuration used, the grain boundary between fuel matrix grains is static, and the change in microstructure is only due to the motion of matrix-bubble interfaces. We assume the motion of the matrix-bubble interfaces is diffusion-limited, and set the non-dimensionalized order parameter mobility  $\bar{L}$  large enough that further increases do not change the observed microstructural evolution. This ensures that the motion of the matrix-bubble interface is diffusion controlled. Using this approach, we set  $\bar{L} = 1$ , which is equivalent to a dimensional value  $L = \frac{\bar{L}}{E^* \tau^*} = 1.59 \times 10^{-10} \text{ m}^3/(\text{J s})$ . The physical parameters used for phase-field simulations are summarized in Table 1.

The non-dimensionalized governing equations were discretized using the MOOSE framework [39]. Hexahedral 3D mesh elements with linear Lagrange shape functions were used for spatial discretization. Mesh adaptivity was used, with three levels of refinement and a minimum element size of  $\Delta x = \Delta y = \Delta z = 10 \text{ nm}$  so that the element size in the interfacial regions is 1/3 of the interfacial width ( $l_{int} = 30 \text{ nm}$ ). No-flux boundary conditions were used in all directions. The second-order backward differentiation formula was used for time integration, and adaptive time stepping was used as implemented in the MOOSE IterationAdaptiveDT time stepper [40].



Parameter	Value
$T$	1035 K
$V_a$	0.03629 nm <sup>3</sup>
$E_v^f$	1.69 eV
$E_v^g$	4.92 eV
$c_g^{b,eq}$	0.3924
$c_v^{b,eq}$	0.6076
$k_v^m = k_g^m$	$5.28 \times 10^{11}$ J/m <sup>3</sup>
$k_v^b = k_g^b$	$8.0 \times 10^{10}$ J/m <sup>3</sup>
$f_0$	$1.82 \times 10^9$ J/m <sup>3</sup>
$\kappa$	$1.92 \times 10^{-8}$ J/m
$m$	$6.84 \times 10^8$ J/m <sup>3</sup>
$\gamma_{mib0}$	1.5
$\gamma_{mimj}$	0.6749
$\dot{F}$	$1.26 \times 10^{13}$ fissions/(cm <sup>3</sup> s)
$Y_{Xe}$	0.2156
$s_g^0$	$2.72 \times 10^{12}$ atoms/(cm <sup>3</sup> s)
$s_v^0$	$2.72 \times 10^{13}$ vacancies/(cm <sup>3</sup> s)
$D_g$	0.1 nm <sup>2</sup> /s
$D_v$	0.1 nm <sup>2</sup> /s
$L$	$1.59 \times 10^{-10}$ m <sup>3</sup> /(J s)

Table 1: Parameters used for phase-field simulations.

## 1.3 Phase-Field Simulations

### 1.3.1 Simulation initial conditions

To investigate the growth of the intergranular bubbles, a planar bicrystal geometry with lenticular bubbles placed on the grain boundary was used for the simulation initial conditions. An example of the initial conditions is shown in Figure 1a. The simulation domain size in the  $x$ ,  $y$ , and  $z$  directions was  $L_x$ ,  $L_y$ , and  $L_z$ , respectively, where  $L_x = 480$  nm,  $L_y = L_z = 2960$  nm. The grain boundary is located at  $x = L_x/2 = 240$  nm. The grain located at  $x < 240$  nm is represented by order parameter  $\eta_{m1}$ , and the grain located at  $x > 240$  nm is represented by order parameter  $\eta_{m2}$ .

The bubbles are represented by the order parameter  $\eta_{b0}$ . In the initial conditions,  $N$  lenticular bubbles with semi-dihedral angle  $\theta/2 = 73^\circ$  [22] are placed at random locations on the grain boundary with a minimum center-to-center distance between bubbles  $l_{min}$ . The initial radius of the bubbles' circular projection onto the grain boundary is 61 nm such that the initial bubble diameter is several times larger than the interfacial width of the phase-field model. The number of bubbles is determined by  $N = n_a A$ , where  $n_a$  is the areal density of bubbles and  $A$  is the area of the grain boundary. Due to the important effect of  $n_a$  shown in Ref. [27], an accurate value must be determined for use in the simulation initial conditions. To do so, the rate theory simulations of Ref. [10] were used. Assuming a truncated octahedron grain geometry with a volume equal to that of a 5  $\mu\text{m}$  diameter spherical grain, the surface area of the space-filling truncated octahedron is  $A_{TO} = 86.3 \mu\text{m}^2$  and its volume  $V_{TO} = 65.4 \mu\text{m}^3$ . From Ref. [10], the number density of grain boundary bubbles  $n_v$  at 1035 K is  $10^{13} \text{ cm}^{-3}$  at 45 GWD/tU. The areal density can be computed

from  $n_a = \frac{V_{TON} n_v}{A_{TO}/2} = 15.2 \mu\text{m}^{-2}$  (where the factor of 2 accounts for the fact that each grain boundary is shared with an adjacent truncated octahedron). Although some concentration of gas atoms and vacancies would have built up in the fuel matrix far from the grain boundary at 45 GWD/tU, diffusional transport of defects to the grain boundary bubbles leads to a region depleted of defect species near the grain boundary. Because of the relatively small size of the simulation domain in the  $x$ -direction, we assume the matrix phase in the simulation domain lies in this depleted region and therefore has a negligible defect concentration in the initial conditions.

### 1.3.2 Simulation results

An example of the simulated microstructural evolution is shown in Fig. 1. For this simulation,  $T = 1035 \text{ K}$ ,  $\theta/2 = 73^\circ$ ,  $n_a = 15/\mu\text{m}^2$ ,  $l_{min} = 160 \text{ nm}$ . The lenticular bubbles in the initial conditions are shown in Fig. 1a. In Fig. 1b, the bubbles have grown, and some bubbles have begun to interconnect with one another. In Fig. 1c, many of the bubbles are interconnected with each other, and most (but not all) of the bubbles are connected to the edge of the simulation domain. At a simulation time of  $1.97 \times 10^8 \text{ s}$ , all the bubbles have connected to one of the edges of the simulation domain; the microstructure at that time is shown in Fig. 1d.

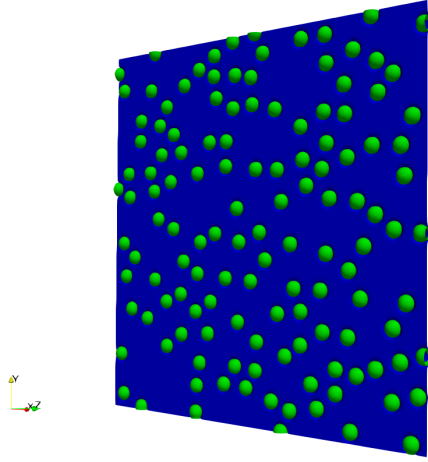
To determine the progress of release of gas from the bubbles, the grain boundary coverage and the fraction of bubbles that are assumed to be vented is calculated by analyzing the phase-field simulation results at each time step. The grain boundary coverage  $X_{GB}^C$  is calculated as the fraction of area on the grain boundary where  $\eta_{b0} > 0.5$ . To calculate the fraction of bubbles that are vented, it is assumed that when a bubble comes into contact with edge of the grain boundary (edge of the simulation domain), it connects to a triple junction network at the edge of that grain boundary (which is not represented explicitly in the simulation), and that the gas within the bubble can then be vented from the fuel. The fraction of bubbles that are vented,  $X_{GB}^V$ , is calculated as the area on the grain boundary that is covered by bubbles that are connected to the edge of the grain boundary divided by the total area covered by the bubble phase.

Figure 2a shows the progress of  $X_{GB}^C$  and  $X_{GB}^V$  versus time for the simulation shown in Figure 1. The increase in both quantities with respect to time is much less rapid than observed in Ref. [27] because vacancies and gas atoms build up slowly from the source terms in the present work, as opposed to existing in the initial conditions as a high initial supersaturation of defects as in Ref. [27]. The areal density of bubbles  $n_a$  is shown as a function of time in Fig. 2b. No bubble coalescence occurs in the early stages of the plot due to the minimum initial spacing  $l_{min}$  imposed in the initial conditions. Once bubble coalescence begins, the rate of bubble coalescence is relatively constant until the bubble density reaches approximately half its initial value, after which the rate of coalescence decreases.

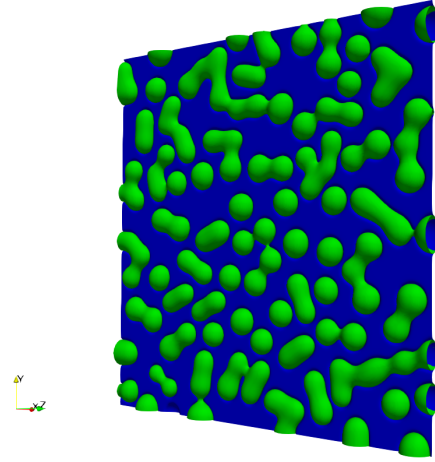
In Figure 2c,  $X_{GB}^V$  is plotted as a function of  $X_{GB}^C$  for the simulation shown in Fig. 1. The rate of venting is relatively slow until  $X_{GB}^C > 0.5$  and increases rapidly until  $X_{GB}^C \approx 0.6$ ; at that point, the rate of venting slows down until venting completes at  $X_{GB}^C = 0.74$ . These results are consistent with the trends observed in Ref. [27].

### 1.3.3 Determination of engineering-scale model parameters from simulation results

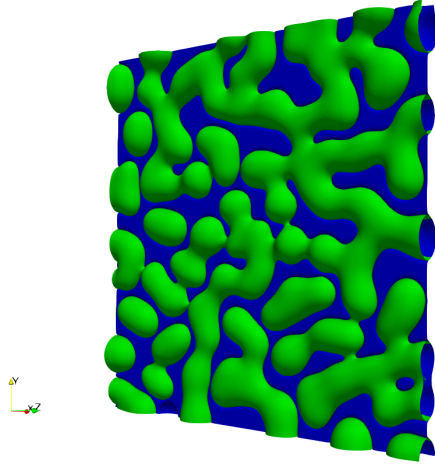
From these simulations, an estimate of  $F_{c,sat}$  can be determined for input to the engineering-scale fuel performance code BISON. As discussed in Section 1.1, the BISON model assumes that when the grain boundary coverage reaches  $F_{c,sat}$ , all the bubbles simultaneously interconnect with each



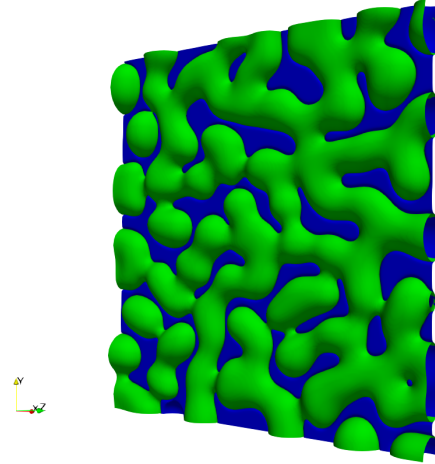
(a) Initial conditions



(b)  $t = 6.04 \times 10^7$  s



(c)  $t = 1.62 \times 10^8$  s



(d)  $t = 1.97 \times 10^8$  s

Figure 1: Evolution of microstructure during simulated growth of grain boundary bubbles in  $\text{U}_3\text{Si}_2$ . The grain boundary is shown in blue and the gas bubbles are shown in green. Simulation temperature  $T = 1035$  K,  $\theta/2 = 73^\circ$ ,  $n_a = 15/\mu\text{m}^2$ ,  $l_{min} = 160$  nm. At  $t = 1.97 \times 10^8$  s, all bubbles have connected to the edge of the simulation domain.

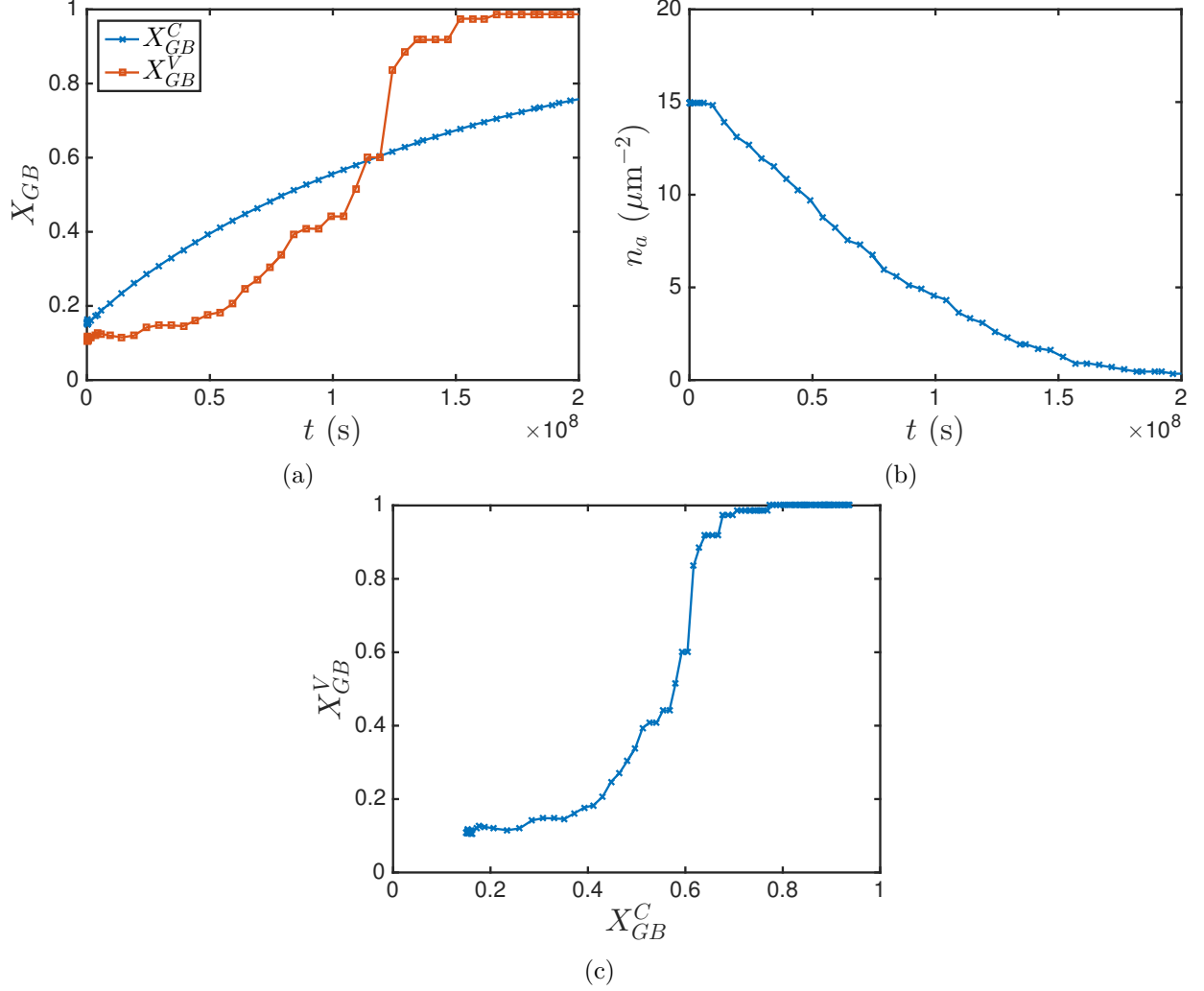


Figure 2: (a) Fractional grain boundary coverage,  $X_{GB}^C$ , and fraction of grain boundary bubbles that are vented,  $X_{GB}^V$ , versus time, for the simulation shown in Figure 1. (b) Areal density of grain boundary bubbles,  $n_a$ , plotted versus time. (c) Plot of fraction of grain boundary bubbles that are vented,  $X_{GB}^V$ , as a function of fractional coverage of the grain boundary by bubbles,  $X_{GB}^C$ .

other and release their gas to the free space between the fuel and cladding. On a plot of  $X_{GB}^V$  versus  $X_{GB}^C$  as in Fig. 2c, this would be represented by a step function, with  $X_{GB}^V = 0$  for  $X_{GB}^C < F_{c,sat}$  and  $X_{GB}^V = 1$  for  $X_{GB}^C \geq F_{c,sat}$ . In Ref. [20], the theoretical value  $F_{c,sat} = 0.78$  was used. To determine an improved estimate from the phase-field simulations, we assume that  $F_{c,sat}$  occurs when the slope of the curve in Fig. 2c is maximum, as this best approximates the step function behavior used in the BISON model. Using this assumption, for the plot in Fig. 2c,  $F_{c,sat} = 0.62$ . With this definition, for this example more than 80% of bubble area is vented when  $F_c = F_{c,sat}$ .

### 1.3.4 Effect of simulation assumptions and parameters on calculated $F_{c,sat}$

In this section, key assumptions involved in the simulations of Section 1.3.2 are considered to determine their effect on the calculated engineering-scale model parameter  $F_{c,sat}$  and to quantify

Configuration	$F_{c,sat}$
1	0.54
2	0.62
3	0.61
4	0.63
5	0.62
<b>Mean</b>	<b>0.60</b>
<b>Standard Deviation</b>	<b>0.036</b>

Table 2: Variation in calculated engineering-scale model parameter  $F_{c,sat}$  for varying initial grain boundary bubble positions. For this set of simulations, the parameters used are the same as those for the simulations shown in Fig. 1, and only the random positions of the bubbles in the initial conditions are varied.

the uncertainty in this calculated parameter.

In physical fuel samples, each grain boundary contains randomly positioned grain boundary bubbles with areal density  $n_a$ . Because of the random positioning of the bubbles on the grain boundary, the curve shown in Fig. 2c is expected to be different for each grain boundary, resulting in a different calculated  $F_{c,sat}$ . To determine the effect of the variation in initial bubble positions on the calculated value of  $F_{c,sat}$ , 4 additional simulations with the same parameters as shown in Fig. 1 were run, but with a different seed in the random number generator used to produce the initial bubble positions along the grain boundary. Thus, the set of  $(y, z)$  positions of the bubble centers in the initial conditions were different for each of the 5 simulations, but the  $x$  position of each bubble remained  $L_x/2$  for each bubble in all simulations. All other simulation parameters and initial conditions remained the same between the 5 simulations. From these simulations, plots of  $X_{GB}^V$  versus  $X_{GB}^C$  were produced, and  $F_{c,sat}$  was calculated for each simulation. The results of these calculations are shown in Table 2. The mean value of  $F_{c,sat}$  was determined to be 0.60 from this set of simulations, with a standard deviation of 0.036. (Although more than five samples should ideally be considered when determining statistical quantities such as the standard deviation, computational resource limitations prevented considering a larger number of samples.) The relatively small standard deviation indicates that the calculated value of  $F_{c,sat}$  is relatively insensitive to the initial bubble position distribution.

The next assumption considered is the minimum spacing between bubbles in the simulation initial conditions,  $l_{min}$ . Although the rate theory simulations used to set the initial conditions allow determination of  $n_a$ , they do not contain information about the spacing between bubbles; therefore they cannot be used to determine a value for  $l_{min}$ . Since the correct value for this parameter is unknown, a set of simulations was conducted to determine how important its effect is on the rate of venting and the value of  $F_{c,sat}$  calculated for input to BISON simulations. Plots of  $X_{GB}^V$  versus  $X_{GB}^C$  for varying  $l_{min}$  are shown in Fig. 3. For  $l_{min} = 130$  nm, the early stages of release are similar to  $l_{min} = 160$  nm. However, the majority of the gas release occurs slightly later, and the value of  $F_{c,sat}$  determined is increased to 0.65 for this set of initial conditions. For a larger value of  $l_{min} = 200$  nm, the early stages of gas release are delayed relative to the  $l_{min} = 130$  nm and  $l_{min} = 160$  nm cases. This is because the larger initial spacing on average delays connections between bubbles until  $X_{GB}^C$  is larger. However, once interconnection begins for the  $l_{min} = 200$  nm case, the rate of interconnection is more rapid in the range  $0.5 < X_{GB}^C < 0.6$ . This is because the initial bubbles are closer to evenly spaced, so once they grow enough to begin interconnecting,

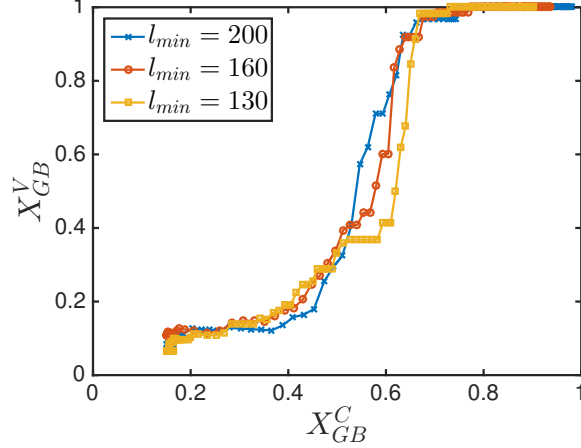


Figure 3: Effect of varying  $l_{min}$  on grain boundary saturation behavior. For a smaller  $l_{min} = 130$  nm,  $F_{c,sat}$  is delayed to 0.65. For a larger  $l_{min} = 200$  nm, in the earlier stages of venting ( $X_{GB}^C < 0.5$ ) venting is delayed compared to the smaller  $l_{min}$  cases, but the rate of increase is more rapid in the range  $0.5 < X_{GB}^C < 0.6$ .

interconnection occurs more rapidly.

To better quantify the effect of varying  $l_{min}$  on  $F_{c,sat}$ , a set of 5 total simulations with different initial random bubble positions were run for the  $l_{min} = 130$  nm and  $l_{min} = 200$  nm cases, similar to the  $l_{min} = 160$  nm case. For the  $l_{min} = 130$  nm simulations,  $F_{c,sat} = 0.61 \pm 0.039$ , while for the  $l_{min} = 200$  nm simulations,  $F_{c,sat} = 0.58 \pm 0.046$ . Thus, recalling that for  $l_{min} = 160$  nm,  $F_{c,sat} = 0.60 \pm 0.036$ , there is a trend of a slight decrease in the mean calculated value of  $F_{c,sat}$  with increase in  $l_{min}$ . This is consistent with the observations of the data shown in Fig. 3 and discussion in the previous paragraph. However, the total variation of  $F_{c,sat}$  is smaller than the standard deviation of each calculated value, so the trend may be merely the result of statistical variation.

The next assumption considered is the simulated grain boundary geometry. For a given grain boundary area, the shape of the grain boundary used in the simulation affects the length of the perimeter of the simulation domain. Because it is assumed that the gas bubbles must connect to the perimeter of the grain boundary to connect to a triple junction that would provide a pathway for gas escape, it is possible that the length of the perimeter could affect the rate of venting. Grain growth simulations in 3D have shown that the average number of edges per grain boundary is greater than 5 [41], so the 4-sided grain boundary used in the present simulations may underestimate the actual rate of venting. To test the effect of grain boundary geometry, we consider the extreme case of a circular grain boundary, which has the maximum perimeter length for a fixed grain boundary area, and compare the results of venting to the square grain boundary geometry.

A set of 5 simulations with a circular grain boundary with the same area and number of bubbles as the previously used square grain boundary was conducted, with  $l_{min} = 160$  nm and other simulation parameters remaining the same as used in the square grain boundary simulations. An example of the microstructure of the gas bubbles in one of these simulations is shown in Fig. 4a, at approximately the same time as the microstructure shown in Fig. 1c. Plots of  $X_{GB}^V$  versus  $X_{GB}^C$  for one example of the circular and square grain boundaries are shown in Fig. 4b. Although some differences are observed, overall the shapes of the curves are quite similar. An average value of  $F_{c,sat} = 0.61 \pm 0.046$  was calculated from the 5 simulations of circular grain boundaries, which is very close to the average value predicted for the square grain boundary of the same area and value of

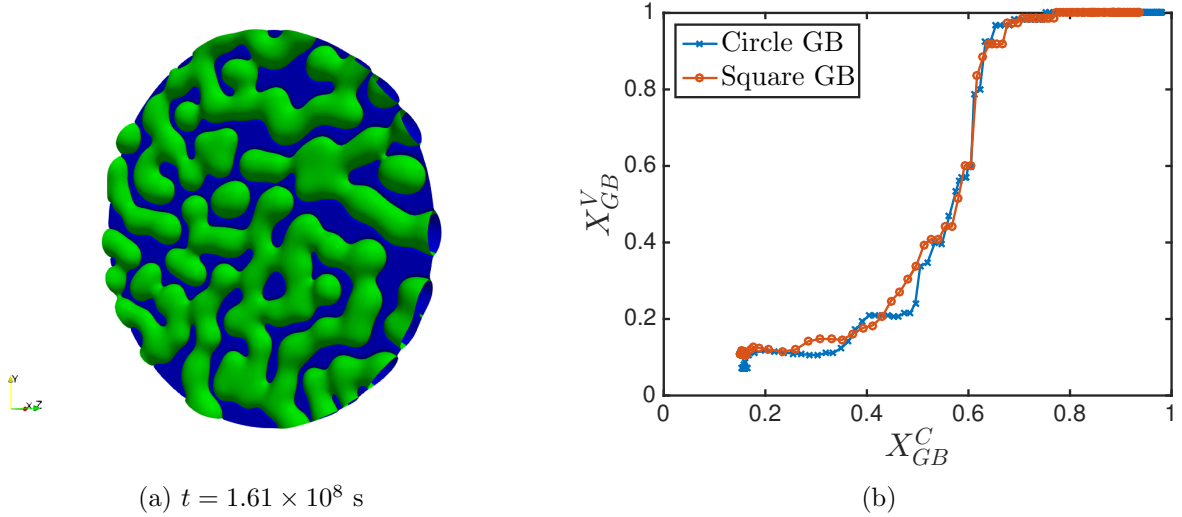


Figure 4: (a) Gas bubble microstructure of circular grain boundary with same simulation parameters as those shown in Fig. 1c, at approximately the same time. (b) Comparison of  $X_{GB}^V$  versus  $X_{GB}^C$  for the square and circular grain boundary geometries. The similarity of the results indicates that the grain boundary geometry does not strongly affect the progress toward venting of the gas bubbles.

$l_{min}$ , which was  $F_{c,sat} = 0.60 \pm 0.036$ . Based on these simulations, we conclude that the geometry of the grain boundary in the simulations does not have a significant effect on the qualitative behavior of venting or the calculated value of  $F_{c,sat}$ .

The final assumption considered is the simulation temperature. The current BISON model of fission gas release and swelling in  $U_3Si_2$  uses a constant value of  $F_{c,sat}$  that does not vary with temperature. The phase-field model used in this work was used to provide insight into whether this is a valid assumption. The simulations described so far were conducted at a temperature of 1035 K, which is representative of the temperature at the center of a fuel pellet at relatively high power. Changes in temperature have the potential to impact many of the parameters used in the phase-field model; however, the impact of temperature on the parameters that have been shown to be important in the progress of venting [27] is quite small. The average grain boundary energy and average bubble-matrix interfacial energy is nearly constant with temperature over the range of temperatures relevant to LWR operation [22], approximately 700K - 1100K. Similarly, the areal density of grain boundary bubbles in the initial conditions determined from simulations is nearly constant over the same range [10].

In the present system, the main simulation parameter that is expected to be strongly impacted by changing temperature is the diffusivity of the defect species. To demonstrate the effect of temperature variation and corresponding defect diffusivity on microstructural evolution, simulations were conducted at  $T = 1015$  K and 1084 K, with corresponding defect diffusivities  $D_v = D_g = 0.05$  nm<sup>2</sup>/s and 0.5 nm<sup>2</sup>/s, respectively, based on atomistic calculations [31, 38]. All other parameters remained as in Table 1, and  $l_{min} = 160$  nm.

As seen in Figure 5, the microstructure is strongly affected by the changes to the defect diffusion coefficient. Higher diffusivities result in a less interconnected microstructure and larger feature sizes with smaller average curvatures for equal simulation times. This is because a higher diffusion coefficient allows the process of coarsening, which is a driving force to reduce interfacial area and average curvature, to proceed with faster kinetics. To evaluate the effect of the change in diffusivities

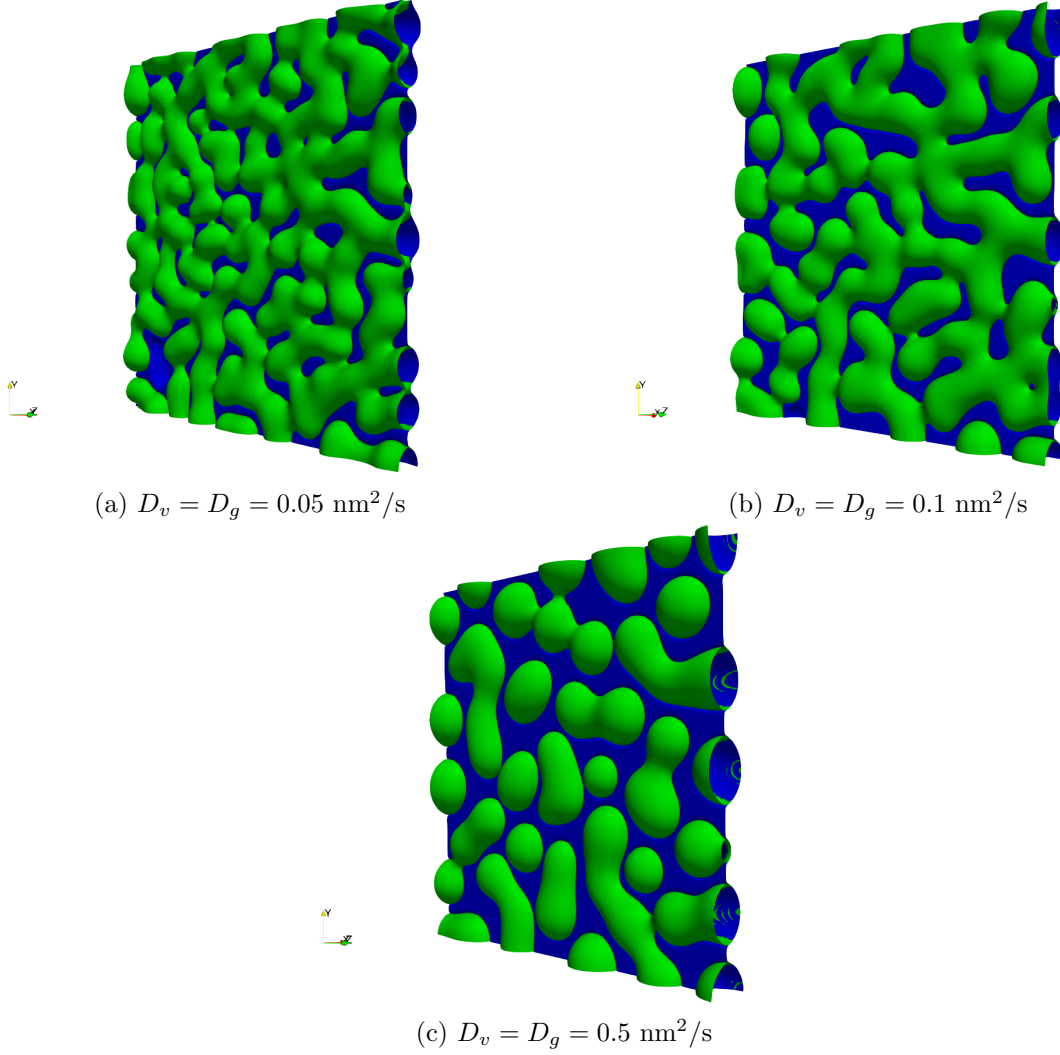


Figure 5: Effect of defect diffusivity on microstructure. Microstructures are shown at time  $t = 1.97 \times 10^8 \text{ s}$ . (a)  $D_v = D_g = 0.05 \text{ nm}^2/\text{s}$ , (b)  $D_v = D_g = 0.1 \text{ nm}^2/\text{s}$ , (c)  $D_v = D_g = 0.5 \text{ nm}^2/\text{s}$ .

on the progress of the gas bubbles toward venting, a set of 5 simulations with  $D_v = D_g = 0.05 \text{ nm}^2/\text{s}$  was conducted, corresponding to  $T = 1015 \text{ K}$ . From these simulations, an average value of  $F_{c,sat} = 0.60 \pm 0.014$  was calculated. So, in spite of the changes in microstructure, the calculated value of  $F_{c,sat}$  was not affected, although the time needed to reach that value of  $F_{c,sat}$  is increased.

Because portions of the fuel are expected to be at  $T < 1015 \text{ K}$ , diffusivities in those portions of the fuel are expected to be lower than the range considered in these simulations. We did attempt to conduct simulations at temperatures lower than  $1015 \text{ K}$ ; however, because of the slower diffusivities, defect concentration increased significantly in the matrix where they are deposited by the source terms, resulting in formation of intragranular fission gas bubbles. Because the model is parametrized to simulate intergranular bubbles, the interface width is much larger than the expected physical size of the intragranular bubbles, and the intragranular bubbles that formed were much larger than the nm-sized bubbles expected in intragranular regions. Therefore, we did not attempt to calculate  $F_{c,sat}$  from these simulations since they do not represent expected physical behavior because of the model parametrization and limitations of the diffuse interface approach.



In summary, we conclude that the calculated value of  $F_{c,sat}$  is unaffected by temperature over the range we were able to consider, but allow that behavior may differ outside that range. Future advances in model formulation and computing power may allow simultaneous consideration of the intergranular and intragranular bubbles with realistic sizes.

### 1.3.5 Comparison with past theoretical and computational results

In this section, we compare the results obtained in our simulations with previous theoretical and computational studies conducted on similar systems. The value of  $F_{c,sat}$  obtained here, 0.60, is significantly lower than the value obtained for a uniform square lattice, 0.78 [26], which is expected based on the uniform lattice's more efficient packing. However, the randomly positioned bubbles in the present simulations more realistically approximate the expected gas bubble microstructure in a fuel pellet.

Significant past effort has been given to determining the percolation threshold of various geometries. In the present context, the percolation threshold  $p_c$  is the grain boundary bubble area fraction at which a path through the bubble phase exists that spans across the entire grain boundary. For a uniform lattice, because all bubbles intersect simultaneously,  $F_{c,sat} = p_c$ . However, in general  $p_c$  should not necessarily be expected to be exactly the same as  $F_{c,sat}$  for randomly positioned bubbles. Comparison with 2D percolation results are most relevant, since percolation in our simulations occurs in the 2D grain boundary plane. The percolation threshold of randomly positioned overlapping circles was determined to be 0.6764 when the circle radii were uniform, and 0.6860 when the radii were non-uniform [42]. A closer approximation to the microstructure obtained in our simulations was found in Ref. [43], which considered the nucleation and growth of precipitates from a supersaturated matrix phase in 2D. In that work, the percolation threshold was determined to be 0.661 (although those results may differ depending on the simulation parameters used and the amount of time the simulation is allowed to run). Thus, the value of  $F_{c,sat}$  determined in the present simulations (and observed experimentally in  $\text{UO}_2$  [24]) is below the value of  $p_c$  determined for the most comparable 2D geometries. This may be due to the fact that the existence of a bubble spanning across the entire grain boundary is not required for all bubbles to connect to a grain edge and thus for the criteria to reach  $F_{c,sat}$  to be met. It may also partially result from the assumptions made in calculating  $F_{c,sat}$ .

The present simulation results can also be compared to the results of Millett et al. for bubble growth by post-irradiation annealing in  $\text{UO}_2$ . Although  $F_{c,sat}$  was not calculated in Ref. [27], it appears from the plots of  $X_{GB}^V$  vs.  $X_{GB}^C$  in that work that similar results would be obtained. This, combined with the consistent values of  $F_{c,sat}$  obtained for different diffusion coefficients in the present work, suggests that the value of  $F_{c,sat} = 0.60$  may be a general result for interconnecting grain boundary bubbles, and not specific to the choice of material parameters or growth mechanism.

## 1.4 Conclusions

To provide mechanistic insights and calculate necessary parameters for engineering-scale modeling of  $\text{U}_3\text{Si}_2$  fuel, a phase-field model of intergranular fission gas bubble growth was parametrized using atomistic and rate theory simulations, and simulations of the growth of bubbles on a grain boundary were performed. The grain boundary coverage and fraction of bubbles that were vented to the edge of the domain were plotted versus time to characterize the progress of venting. The progress of these quantities versus time was much slower than previous simulations in  $\text{UO}_2$  fuel, due to the fact that the  $\text{UO}_2$  fuel simulations used an initial supersaturation of gas atoms in the initial conditions and were thus more representative of post-irradiation annealing. When the fraction of

vented bubbles was plotted versus the grain boundary coverage by bubbles, the results were similar to the previous  $\text{UO}_2$  simulations. (However,  $F_{c,sat}$  was not calculated from the  $\text{UO}_2$  simulations, so only qualitative comparisons are possible.)

From the phase-field simulation results, the parameter  $F_{c,sat}$  (saturation coverage of grain boundaries) for the current BISON fuel performance model was determined. For the nominal set of simulation parameters,  $F_{c,sat} = 0.60 \pm 0.036$ , calculated from the  $F_{c,sat}$  for 5 configurations of randomly placed initial bubble positions. The effect of important model assumptions and uncertain simulation parameters on the calculated value of  $F_{c,sat}$  was considered. Larger values for  $l_{min}$ , the initial spacing between bubbles, resulted in a small decrease in the calculated  $F_{c,sat}$ ; however, the trend may be only the result of statistical variation. The geometry of the grain boundary in the simulations was found to not have a significant effect on the calculated value of  $F_{c,sat}$ . Simulation temperature was also found to not have a significant effect on the calculated value of  $F_{c,sat}$ , although it did affect the microstructure. However, the range of temperatures considered does not cover the full range of temperatures that would be experienced by  $\text{U}_2\text{Si}_2$  fuel due to limitations of the current model parametrization.  $F_{c,sat}$  was slightly smaller than the percolation threshold for the most comparable 2D geometries considered in past work. The similarity of the present results to the findings of Ref. [27] and the consistent values of  $F_{c,sat}$  determined for different diffusion coefficients suggests that  $F_{c,sat} = 0.60$  may be a generally applicable result for interconnecting grain boundary bubbles.

The phase-field simulations described in this work also provide insight for future improvements to the engineering-scale swelling and fission gas release model described in Ref. [20]. The simulations show that gas release occurs over a range of values of grain boundary coverage, rather than with a rapid step function change at a single value as the current model assumes. Therefore, future work in BISON should focus on incorporating a gradual release of gas according to curves calculated by Marmot simulations, but only after a percolated triple junction network is formed [23].

## 2 Mechanistic Grain Growth Model for Fresh and Irradiated $\text{UO}_2$ Nuclear Fuel

### 2.1 Introduction

Grain growth plays a significant role in the life of light water reactor (LWR) uranium dioxide ( $\text{UO}_2$ ) fuel pellets. During fuel pellet fabrication via sintering, the grain structure coarsens due to grain growth, resulting in an average grain size typically around ten microns. During reactor operation, significant grain growth occurs in the hotter portions of the fuel pellet, near its center, and the average grain size reaches several times its initial value. This change in grain size significantly impacts fuel performance, since the grain size affects various aspects of the overall behavior of the fuel, including fission gas release [44, 45], fracture [46], and heat conduction [47].

The grain growth of  $\text{UO}_2$  has been studied for many years, using both in- and out-of-pile experiments. The resultant data have significant scatter and have been analyzed in various ways [7, 48]. The large scatter in the reported grain growth during thermal annealing of unirradiated  $\text{UO}_2$  results from the sensitivity of grain growth to the stoichiometry, which is difficult to control, and to the porosity of the sintered samples.  $\text{UO}_2$  grain growth becomes even more complicated during reactor operation. The stoichiometry changes, sintered porosity decreases, and solid fission products and fission gas bubbles form, all of which impact grain growth. Many semi-empirical models have been developed for grain growth in unirradiated  $\text{UO}_2$  [7, 48]. These depend on the initial grain size and the temperature but are independent of the porosity. Only a few semi-empirical models have been developed for in-reactor grain growth [7, 49], and the oldest is still the most commonly used [7]. The predicted grain growth in this model is a function of initial grain size, temperature, and burnup.

Mechanistic models of grain growth explicitly describe the physical behaviors of grain boundary (GB) migration using parameters with real physical meaning, while semi-empirical models employ equations for which the form has some physical justification but includes parameters without physical meaning that are obtained by fitting to data. A major benefit of mechanistic models is that they can be applied to many materials, as long as the physical parameters are known. As far as the authors are aware, no mechanistic models have been developed to predict the change in the average grain size of  $\text{UO}_2$  with time, though the semi-empirical model from Ainschough et al. [7] comes the closest. There have been a number of numerical simulation methods developed to model  $\text{UO}_2$  grain growth at the mesoscale, in which the individual grains are resolved. Some have looked at pure curvature driven grain growth [50], while others have included additional driving forces [51] or pinning by porosity [52, 53, 54, 55].

In this work, we present a new, mechanistic model that predicts the increase in the average grain size for both unirradiated and irradiated  $\text{UO}_2$ . The average grain size is predicted as a function of the initial grain size, temperature, evolving sintered porosity, and fission gas bubble fractional coverage. The model parameters are the average GB energy and mobility in  $\text{UO}_2$ , as well as the pore mobility. In this paper, we begin by summarizing the relevant grain growth theory in Sec. 2.2. Then, in Sec. 2.3, we present new fits of data from the literature for the GB energy and mobility. We present our new mechanistic model in Sec. 2.4 and, in Sec. 2.5, validate it against experimental data. Finally, in Sec. 2.6, we implement the model in the BISON fuel performance code and quantify its impact on the predicted behavior for steady and transient power cases.

## 2.2 Grain Growth Theory

GBs migrate to reduce the overall free energy of the material. The velocity at a specific location on a GB  $v_g$  can be described as

$$v_g = M_g[F_g - P_g]^+, \quad (33)$$

where  $M_g$  is the GB mobility at the location, and  $F_g$  and  $P_g$  are the driving and resistive forces per unit area at the location, respectively. The  $[x]^+$  operator is equal to  $x$  when  $x > 0$  but is equal to zero when  $x \leq 0$ . Various driving forces for GB migration can occur, including GB energy, elastic energy, plastic energy, and temperature gradients. The GB energy driving force, often called the curvature driving force, is the most common, while the temperature gradient driving force has been found to be negligible for temperature gradients commonly experienced in both LWR and fast reactor oxide fuels [51]. The curvature driving force is defined as

$$F_g = \frac{\gamma_g}{R_g}, \quad (34)$$

where  $\gamma_g$  and  $R_g$  are the GB energy and radius of curvature at the GB location, respectively. The resistive force results from defects that impede GB migration, such as second phase particles or porosity. GB properties, such as the energy and mobility, are highly anisotropic, depending on the misorientation of grains on either side of the GB and on the inclination of the GB.

The migration of individual GBs causes some grains to shrink and disappear and others to grow. This results in an increase of the average grain size with time, commonly called grain growth. The GB anisotropy affects the motion of individual GBs and will impact which grains grow and shrink, but typically does not impact the average grain growth rate [56]. Therefore, when predicting the change in the average grain size, we can often neglect the anisotropy and focus on the average GB mobility and energy. If we consider a polycrystal in which the average grain size  $\bar{D}$  and the average GB curvature  $\bar{R}$  are related by a geometric constant  $\alpha$  such that  $\bar{D} = \alpha^{1/2}\bar{R}$ , then the change in the average grain size with time is

$$\frac{\partial \bar{D}}{\partial t} = \alpha^{1/2} \frac{\partial \bar{R}}{\partial t} \approx \alpha \bar{M} \frac{\bar{\gamma}}{\bar{D}}, \quad (35)$$

where  $t$  is the time and  $\bar{M}$  and  $\bar{\gamma}$  are the average GB mobility and energy for the material. Here, we have approximated the change in the average curvature using the velocity of an average GB as defined by Eq. (33) with only the curvature driving force and no resistive forces. If we assume that the average GB mobility and energy are constant, we can then integrate Eq. (35) to obtain

$$\bar{D}^2 - \bar{D}_0^2 = 2\alpha \bar{M} \bar{\gamma} t, \quad (36)$$

where  $\bar{D}_0$  is the initial average grain size. 3D grain growth simulations that only represent the curvature driving force produce results in good agreement with this expression [57, 58], as do experiments near the melting temperature [59].

In many polycrystal grain growth experiments, including both metals and ceramics, the grain growth is not accurately described by Eq. (36). Therefore, a semi-empirical equation is often used to describe the growth behavior, i.e.

$$\bar{D}^n - \bar{D}_0^n = Kt, \quad (37)$$

where the exponent  $n$  and the rate constant  $K$  are determined by fitting to experimental data. Values for the exponent  $n$  that best fit the data vary, ranging from 2 to 4 [59]. When  $n = 2$ , Eqs. (36) and (37) can be equated, giving  $K = 2\alpha \bar{M} \bar{\gamma}$ ; however, this is not the case for any other

value of  $n$ . The value of  $n$  has been shown to vary with porosity, impurities, residual stress, and more [59]. Equation (36) does not accurately describe the grain growth behavior in these cases because the assumptions used to derive the model are not true, i.e. that the curvature is the only significant driving force and that there are no significant resistive forces. For example, in a material with significant residual stress, the elastic and plastic driving forces would be significant in addition to the curvature; in a material with porosity or second phase particles, there would be significant resistive forces. It is important to note that when Eq. (37) is used with  $n \neq 2$ , the model is semi-empirical and it cannot be used to determine grain growth in a given material without data for fitting.

An alternative approach to modeling normal grain growth in materials with significant resistive force is to include the resistive force in Eq. (35), i.e.

$$\frac{\partial \bar{D}}{\partial t} = \alpha \bar{M} \bar{\gamma} \left( \frac{1}{\bar{D}} - \frac{\bar{P}}{\alpha^{1/2} \bar{\gamma}} \right), \quad (38)$$

where  $\bar{P}$  is the average resistive force per unit area. Note that this equation still assumes that curvature is the only significant driving force. The resistive force can be estimated for second phase particles or porosity if the average radius of the porosity or second phase particles and the fraction of the GB area covered (the fractional coverage) are known [53]. The fractional coverage is difficult to obtain from experimental data; however, for any resistive pressure there will exist a maximum average grain size at which the driving force will equal the resistive pressure. This maximum grain size  $\bar{D}_m = \bar{P}/\alpha^{1/2} \bar{\gamma}$ , such that

$$\frac{\partial \bar{D}}{\partial t} = k \left( \frac{1}{\bar{D}} - \frac{1}{\bar{D}_m} \right), \quad (39)$$

where the rate constant  $k = \alpha \bar{M} \bar{\gamma}$ . Note that the rate constant  $k$  is twice the rate constant  $K$  used in Eq. (37) for cases with  $n = 2$ . Assuming  $\bar{D}_m$  is constant, Eq. (39) can be integrated to give

$$\bar{D}_m (\bar{D}_0 - \bar{D}) + \bar{D}_m^2 \ln \left( \frac{\bar{D}_m - \bar{D}_0}{\bar{D}_m - \bar{D}} \right) = kt. \quad (40)$$

However, if  $\bar{D}_m$  is not constant (the average radius and/or fractional coverage of the porosity or second phase particles changes with time), the integral would need to be carried out numerically. This form simplifies the comparison with experimental data, as the maximum average grain size can often be estimated or fit.

Typical UO<sub>2</sub> grain growth experiments use sintered samples that are not fully dense. Therefore, there is porosity, and the resistive pressure is not zero. UO<sub>2</sub> grain growth data has most often been analyzed using Eq. (37), and the rate constant is defined with an Arrhenius expression as  $K = K_0 \exp(-\frac{Q}{RT})$ , where  $K_0$  is the rate constant prefactor,  $Q$  is the activation energy,  $R$  is the ideal gas constant, and  $T$  is the temperature in K. Annealing data for unirradiated UO<sub>2</sub> have been used to determine values for  $n$ ,  $K_0$ , and  $Q$ , with the exponent  $n$  ranging from 2.5 to 4.0 [48] for the various data. However, even when various data were fit with the same exponent  $n$ , the corresponding  $Q$  values varied by as much as 50%, and the  $K_0$  values varied by as much as nine orders of magnitude. Only Ainscough et al. [7] have analyzed UO<sub>2</sub> grain growth data using Eq. (40). They fit values for  $k = k_0 \exp(-\frac{Q}{RT})$  and  $\bar{D}_m$ . They also fit a value for  $\bar{D}_m$  that decreases with increasing burnup for use with irradiated fuel. Their semi-empirical model is the most widely used to predict the change in UO<sub>2</sub> grain size in fuel performance codes [60].

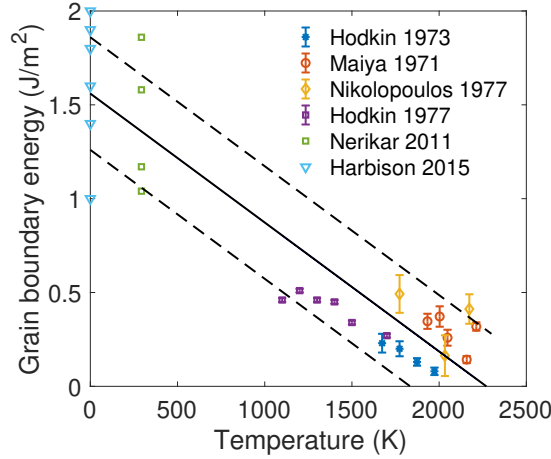


Figure 6: GB energy values for  $\text{UO}_2$  from measurements in the 1970s [1, 2, 3, 4] and more recent MD simulations [5, 6]. Note that the values shown from Ref. [6] are representative values from the hundreds of energies calculated. We also show a linear fit with temperature as a solid black line that we recommend as a reasonable value for the average  $\text{UO}_2$  GB energy. The dashed lines show the uncertainty limits of the fit.

## 2.3 Average GB Energy and Mobility in $\text{UO}_2$

Our new mechanistic model of grain growth in  $\text{UO}_2$ , like all mechanistic models, requires some estimate of the GB mobility and energy. While all of the mesoscale numerical simulation methods developed to model  $\text{UO}_2$  have used GB mobility and energy values found in the literature, the selected values have varied widely. Therefore, we begin by surveying and discussing the various values available for the average GB energy and mobility for  $\text{UO}_2$ .

### 2.3.1 Grain boundary energy

The GB energy of  $\text{UO}_2$  was measured using thermal groove experiments by various researchers in the 1970s [1, 2, 3, 4], and the values are summarized in Fig. 6. These measurements targeted individual GBs arbitrarily selected from the surface, but their misorientations were not characterized. These GB energy values were fairly consistent, though they showed some scatter, possibly due to measurement error and variation in the misorientation of the selected GBs. They were also shown to vary with stoichiometry. All of the measured GB energy values decreased fairly linearly with temperature.

The energies of various  $\text{UO}_2$  GBs have also been calculated with molecular dynamics (MD) simulations using the Basak potential [61] at room temperature [5] and at 0 K [6]. Nerikar et al. [5] selected four GBs found to be common in sintered  $\text{UO}_2$  from electron backscatter diffraction data. Harbison [6] calculated the energies for hundreds of GBs in order to fit a continuous function to the data. The simulated values are much higher than the measured values, but when plotted with the experimental values, as done in Fig. 6, it is clear that they follow the same general trend with temperature.

For convenience in modeling, we have created a linear fit to the experimental data shown on Fig. 6 to obtain a value for the average GB energy  $\bar{\gamma}$ . The equation for the fit in terms of the

temperature  $T$  in K is

$$\bar{\gamma}(T) = (1.56 - 5.87 \times 10^{-4}T) \pm 0.3 \text{ J/m}^2, \quad (41)$$

where the uncertainty limits were set to encompass the majority of the experimental data. Our proposed fit corresponds well with the values calculated using the MD simulations. The reason for the linear dependence with temperature is unclear, though it could be due to entropy.

### 2.3.2 Grain boundary mobility

The GB mobility cannot be directly measured from experiments because it is always convoluted with the driving force. When only the curvature driving force is significant, the mobility is convoluted with the GB energy giving the reduced mobility  $\bar{M} = \bar{\gamma}\bar{M}$ . The reduced mobility can be measured for individual GBs using bicrystal samples with specific geometries [62, 63], but these approaches have never been applied to  $\text{UO}_2$ . Alternatively, polycrystalline samples can be annealed and the average grain size can be measured over time.

In order to extract the GB mobility from polycrystal measurements of the average grain size, the data must first be fit to a grain growth model such as Eq. (37) or Eq. (40). When the data is fit using Eq. (37), the rate constant  $K$  is sometimes converted to the GB mobility using the expression [64]:

$$\bar{M} = \frac{K}{n\bar{\gamma}\bar{D}^{n-2}}. \quad (42)$$

Thus, when the exponent  $n = 2$ ,  $\bar{M} = K/(2\bar{\gamma})$ , which assumes that the geometric constant  $\alpha = 1$ . When the exponent  $n > 2$ , this expression results in a value for the GB mobility that depends on the average grain size. However, as we have established previously, the exponent  $n > 2$  signifies that there are other driving forces and/or significant pinning forces present in the material. Thus, the mobility calculated using Eq. 42 for  $n > 2$  is actually an effective mobility that also includes other effects.

When data is fit using Eq. (40), the rate constant can always be converted to the true mobility using the expression  $\bar{M} = k/\bar{\gamma}$ , assuming  $\alpha = 1$ . The actual value for the geometric constant  $\alpha$ , which relates the average grain size with the average grain curvature, will vary depending on the shape of the grains and could vary between materials. Mesoscale simulations of GB migration in polycrystals using the phase field method (assuming isotropic GB properties) found  $\alpha = 1/2$  in 2D simulations [51] and  $\alpha = 1.0$  in 3D simulations [65]. More study is needed to determine the accuracy of the assumption that  $\alpha = 1$ .

We determine an expression for the average GB mobility for  $\text{UO}_2$  from values for the rate constant  $k$  that were determined from multiple samples annealed at various temperatures by Ainscough et al. [7]. However, these rate constants were determined using average grain sizes that were measured using the linear intercept method without modification. The linear intercept  $\bar{l}$  is not equivalent to the grain size; according to ASTM standard 112-13, the average grain size  $\bar{D} = 1.571\bar{l}$ . Thus, the linear intercept rate constants  $k$  from that work must be multiplied by the same factor to convert them to grain size rate constants. We have taken the rate constants from Ainscough et al. and converted them to grain size rate constants and then to mobilities using  $\bar{M} = k/\bar{\gamma}$  with GB energies calculated from Eq. (41). We then fit an Arrhenius expression to the mobilities to determine values for  $M_0$  and  $Q$ :

$$\bar{M} = M_0 \exp\left(-\frac{Q}{RT}\right). \quad (43)$$

In order to obtain reasonable fits for  $M_0$  and  $Q$ , mobilities from multiple temperatures should be used. Ainscough et al. [7] determined rate constants for twelve batches of  $\text{UO}_2$  samples, each

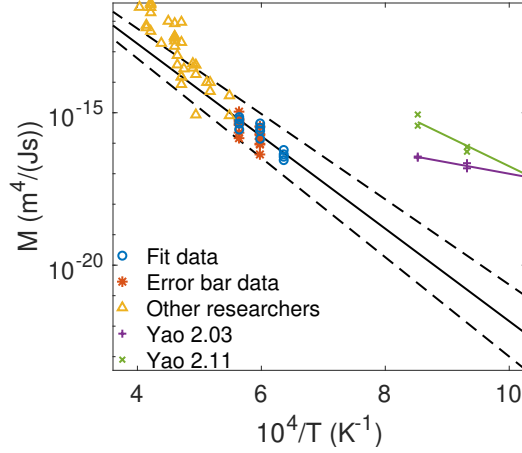


Figure 7: Our fit of the average  $\text{UO}_2$  GB mobility using data from Ainscough et al. [7]. The fit (solid black line) was determined from mobility values converted from rate constants for the four batches with values from three temperatures (labeled “Fit data”). The uncertainty limits (dashed black lines) were determined using data from the other eight batches (labeled “Error bar data”). Data from other researchers taken from Tab. 11 in Ref. [7] are shown for comparison. Data from Yao et al. [8] and the corresponding mobility fits are also shown.

with different initial densities and grain sizes. Rate constants were obtained at three temperatures for four of the batches, but at only two temperatures for the other eight batches. We determined the values for our Arrhenius fit using the four batches with data for three temperatures. We then determined uncertainty limits on the fit values by comparing predictions to the data from the remaining eight batches. Our determined values are  $M_0 = 2.14 \pm 0.15 \times 10^{-7} \text{ m}^4/(\text{Js})$  and  $Q = 290 \pm 22 \text{ kJ/mol} = 3.01 \pm 0.23 \text{ eV}$ . The mobility values, our Arrhenius fit, and the uncertainty are shown in Fig. 7. The fit is compared to data from five other researchers for which Ainscough et al. calculated rate constants, taken from Tab. 11 in Ref. [7]. The uncertainty limits of the fit encompass the majority of the data. All but one of the data points outside the uncertainty limits fall above the upper limit. Ainscough et al. suggest that these samples may be hyperstoichiometric due to issues with the methods used to control the stoichiometry.

A much more recent study from Yao et al. has investigated the grain growth in nanocrystalline  $\text{UO}_2$  pellets that were fabricated using spark plasma sintering [8]. They focused on hyperstoichiometric samples, using samples of  $\text{UO}_{2.03}$  and  $\text{UO}_{2.11}$  with initial grain sizes ranging from 63 nm to 165 nm and porosities ranging from 1.3% to 4.0%. They annealed the samples at 700, 800, and 900°C and ensured that the stoichiometry did not change during annealing. They analyzed the data by fitting a rate constant and grain size exponent, similar to Eq. 37, but they also fit an exponent on the time. Thus, their analysis cannot be directly compared with that from Ainscough et al. [7]. Therefore, we have reanalyzed the data here using Eq. (40) to calculate the mobility for  $\text{UO}_{2.03}$  and  $\text{UO}_{2.11}$ , and the results and mobility fit are shown in Fig. 7. The mobilities ( $\text{m}^4/(\text{Js})$ ) are

$$\bar{M}_{2.03} = 5.00 \times 10^{-14} \exp\left(-\frac{0.73 \text{ eV}}{k_b T}\right), \quad (44)$$

$$\bar{M}_{2.11} = 1.18 \times 10^{-7} \exp\left(-\frac{1.95 \text{ eV}}{k_b T}\right). \quad (45)$$



These results show that the GB mobility increases with hyperstoichiometry, which has also been observed by other researchers. However, the activation energy for the mobility is much smaller than those obtained by our analysis and the analyses of other researchers using standard fuel pellets with larger grain sizes (0.73 eV and 1.95 eV versus  $3.0 \pm 0.21$  eV). Yao et al. [8] hypothesize that the small activation energies are due to the small grain sizes. However, as mentioned previously, the GB mobility should be independent of the grain size. An alternative explanation is that GB curvature is not the only significant driving force, e.g. there may be significant residual stress. If this is the case, then Eq. (40) cannot be used to determine the mobility.

MD simulations have also been used to calculate the GB mobility for  $\text{UO}_2$ . Bai et al. [66] calculated the GB mobility with MD using three different approaches. For all three approaches, the GB mobilities that were determined were many orders of magnitude higher than experimental values. These results illustrate a general issue with GB mobilities calculated using MD: MD calculates the intrinsic GB mobility for a perfect material without defects or impurities. Such defects in real materials have been shown to severely reduce the GB mobility [67].

Another approach used to determine the GB mobility is an analytical equation [64]:

$$\bar{M} = \frac{f D_b \Omega}{\delta_g R T}, \quad (46)$$

where  $D_b$  is the diffusion coefficient of the slower ion across the GB (the U ion in  $\text{UO}_2$ ),  $f$  reflects the density of boundary core sites associated with high jump probabilities and is equal to one for high angle boundaries,  $\Omega$  is the molar volume, and  $\delta_g$  is the GB width. The diffusion coefficient  $D_b$  is typically assumed to be one or two orders of magnitude below the GB diffusion coefficient, though its actual value is rarely known. This is complicated in  $\text{UO}_2$  because there is some discrepancy in the value of the diffusion coefficient for U ions along GBs; values measured in the 1960s are five orders of magnitude larger than values measured in 2000. This is likely due to issues in the measured bulk diffusion coefficient [68]. Equation (46) has been used to calculate the GB mobility of  $\text{UO}_2$  using a value for the U ion diffusion coefficient from the 1960s (reduced by one order of magnitude) [52], though the calculated value was roughly two orders of magnitude larger than the value from our fit using the data from Ainscough et al. [7]. We have recalculated the mobility using the smaller value from Ref. [68], giving a mobility that is three orders of magnitude smaller than our fit value. Thus, due to the large uncertainty in the value of  $D_b$ , this equation may not be an accurate means of determining the GB mobility in  $\text{UO}_2$ .

While Eq. 46 is not an accurate means of determining the GB mobility, it does provide important insights. In the equation, GB mobility is a linear function of the U ion GB diffusivity. Self diffusion is a linear function of the vacancy concentration for ions that diffuse via vacancy diffusion. Under thermal conditions, this makes the self diffusion a function of the vacancy equilibrium concentration and thus the formation energy of vacancies. However, in reactor conditions, the vacancy concentration will be elevated, accelerating self diffusion. Thus, the GB mobility may also be a linear function of the vacancy concentration and be elevated in reactor conditions.

## 2.4 Grain Growth Model with Porosity

The objective of our new grain growth model is to predict the evolution of the average grain size at a specific material point of  $\text{UO}_2$ . The evolution should be a function of the temperature, the average GB energy and mobility of the material, as well as various types of porosity within the material. Thus, it must account for various physical phenomena, as summarized in the following subsections.

### 2.4.1 Model of the Resistive Force

The resistive force ( $\bar{P}$  in Eq. (38)) of static particles/pores on GBs was first studied by Zener, assuming a single average particle/pore radius and randomly positioned particles/pores. It has since been expanded to consider deviations from random positioning [69]. The average resistive force per unit area is

$$\bar{P} = \frac{3}{2} R \frac{\bar{\gamma} f_V}{r_p}, \quad (47)$$

where  $r_p$  is the particle/pore radius,  $f_V$  is the volume fraction of the particles/pores, and  $R$  is a stereological parameter that defines how many times more likely a particle/pore is to be found touching a GB than if they were randomly positioned. The determination of the resistive force is simplified if information is known directly about the particles/pores in contact with GBs [51]. If the fraction of the GB area covered by particles/pores  $f_c$  is known, then

$$\bar{P} = \frac{\bar{\gamma} f_c}{r_p}. \quad (48)$$

If the number of particles/pores per unit GB area  $N_p$  is known, then

$$\bar{P} = \bar{\gamma} \pi N_p r_p. \quad (49)$$

$f_c$  and  $N_p$  are related according to  $N_p = f_c/(\pi r_p^2)$ . Note that these expressions assume that all of the particles/pores are spherical and the same size.

Due to variation in the pore size, the resistive force becomes a function of a random variable and will also vary. However, there are discrepancies in the literature regarding the impact of a particle/pore size distribution on the average resistive force. Researchers have used simulation and statistical analysis to investigate the impact of a size distribution, with one work indicating that it will increase the average resistive force [70] and another concluding that it will have no effect [71]. A third work predicted that the presence of a particle/pore size distribution will decrease the average resistive force [51], but this was due to an error in the statistical analysis.

The discrepancy is due, at least in part, to the assumptions regarding which parameters are treated as deterministic and which are treated as random variables. If the value of  $r_p$  varies but  $f_c$  and  $R$  are assumed to be constant (making  $N_p$  vary due to the variation of  $r_p$ ), then Eq. (47) becomes a function of the expected or mean value  $E(1/r_p)$  as follows:

$$\bar{P} = \frac{3}{2} R \bar{\gamma} f_V E\left(\frac{1}{r_p}\right). \quad (50)$$

The expected value of the inverse of a random variable tends to increase with the standard deviation of the random variable. Thus, in this case, the average resistive force would increase as the standard deviation of  $r_p$  increases. If  $r_p$  varies and  $f_c$  is assumed to not vary, then Eq. (48) also becomes a function of  $E(1/r_p)$ , and the resistive pressure will again increase as the standard deviation of  $r_p$  increases. However, if  $r_p$  varies and  $N_p$  is assumed to be constant (making  $f_c$  and  $f_V$  vary due to the variation of  $r_p$ ), then Eq. (49) becomes a function of the expected or mean value of  $r_p$ , and the average resistive force will be constant as the standard deviation of  $r_p$  increases.

Porosity in  $\text{UO}_2$  typically comes in the form of pores left over after sintering (typically defined by their volume fraction  $f_V$ ) or in the form of fission gas bubbles (with their GB fractional coverage  $f_c$  predicted by a fission gas release model). Thus, Eqs. (47) and (48) are the most useful expressions for defining the pinning force in  $\text{UO}_2$ . Both sintered porosity and fission gas bubbles will always have a distribution of sizes. Therefore, it is important that we consider the impact of a size distribution

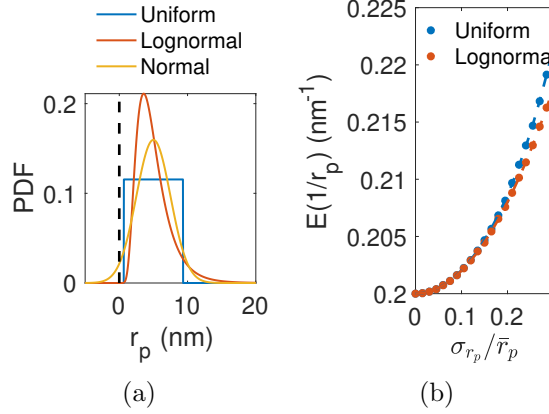


Figure 8: Demonstration of the impact of a pore size distribution. (a) demonstrates that it is not possible to guarantee radii above zero when using a normal distribution by showing the probability density function (PDF) for a pore radius that follows a uniform, lognormal, and normal distribution. (b) compares the expected value of the inverse of the pore radius versus the ratio of the pore radius standard deviation to the mean from uniform and lognormal distributions. Both plots were made assuming an average pore radius  $\bar{r}_p = 5$  nm

on the pinning force. For that, we need to define the expected value of the inverse of the pore radius, as shown in Eq. (50). The expected value depends on the distribution of the pore radius, and in this work we will consider two distributions: uniform and lognormal. We will not consider a normal distribution because there is always some probability that normally distributed radii could take on negative values, which are non-physical, as illustrated in Fig. 8a. The expected value of the inverse of the two distributions with a mean of  $\bar{r}_p$  and a standard deviation  $\sigma_{r_p}$  are

$$E\left(\frac{1}{r_p}\right) = \frac{\ln r_{mx} - \ln r_{mn}}{r_{mx} - r_{mn}}, \quad (51)$$

for a uniform distribution, where  $r_{mn} = \bar{r}_p - \sqrt{3}\sigma_{r_p}$  and  $r_{mx} = \bar{r}_p + \sqrt{3}\sigma_{r_p}$ , and

$$E\left(\frac{1}{r_p}\right) = e^{-\mu + \sigma^2/2}, \quad (52)$$

for a lognormal distribution, where  $\mu = \ln(\bar{r}_p^2 / \sqrt{\bar{r}_p^2 + \sigma_{r_p}^2})$  and  $\sigma^2 = \ln(1 + \sigma_{r_p}^2 / \bar{r}_p^2)$ . The expected values from these two distributions for the inverse of a varying pore radius are compared for various standard deviations in Fig. 8b.

## 2.4.2 Model of Pore Mobility

Pinning models predict that once the resistive force is equal to the driving force, GB motion stops. However, just as the particles/pores assert a resistive force on the GB, the GB also asserts an equivalent force on them. Thus, if they are mobile, such as in the case of pores, then the GB can drag them along at a velocity of

$$v_p = P \frac{M_p}{N_p}, \quad (53)$$

where  $N_p$  is the number of pores per unit GB area, and  $M_p$  is the pore mobility (with different units than the GB mobility) [64]. For spherical pores that migrate due to surface diffusion, the pore mobility is defined as

$$M_p = \frac{D_s \delta_s \Omega}{RT \pi r_p^4}, \quad (54)$$

where  $D_s$  is the surface diffusivity, and  $\delta_s$  is the thickness of the surface layer. The expression changes for other migration mechanisms, but in all cases, it is a function of  $1/r_p^n$ , where  $n = 4$  for surface diffusion,  $n = 3$  for lattice diffusion, and  $n = 2$  or  $3$  for vapor transport [64].

The expression for the pore mobility from Eq. (54) assumes that all pores are the same size. Therefore, we must modify Eq. (54) so that it accounts for a varying pore size. When we consider the pore radius as a random variable, the pore mobility  $M_p$  becomes a random function that also follows a distribution. Its expected or mean value becomes

$$E(M_p) = \frac{D_s \delta_s \Omega}{RT \pi} E(r_p^{-4}). \quad (55)$$

Unfortunately, there is no closed form solution for the expected value of the inverse of random variable raised to the fourth power. Therefore, we have developed an empirical model of  $E(r_p^{-4})$  by fitting to results from Monte Carlo simulations using a uniform and a lognormal distribution of the pore radii. We defined the empirical model as

$$E(r_p^{-4}) = \bar{r}_p^{-4} p_4 \left( \frac{\bar{r}_p}{\sigma_{r_p}} \right), \quad (56)$$

where  $p_4 \left( \frac{\bar{r}_p}{\sigma_{r_p}} \right)$  is a fourth-order polynomial function of the mean bubble radius divided by its standard deviation. We fit the polynomial to five million values of  $r_p^{-4}$ , in which the values of  $r_p$  were sampled from the given distribution with  $\bar{r}_p = 1 \mu\text{m}$  and standard deviation values up to  $\sigma_{r_p} = 0.3\bar{r}_p$ . The fitted functions for the two distributions are

$$p_4^{uni} = 333.8a^4 - 109.9a^3 + 25.2a^2 - 0.7a + 1.0, \quad (57)$$

$$p_4^{logn} = 103.4a^4 - 21.9a^3 + 12.9a^2 - 0.1a + 1.0, \quad (58)$$

where  $p_4^{uni}$  and  $p_4^{logn}$  are the polynomial functions for the uniform and lognormal distributions, respectively, and  $a = \bar{r}_p/\sigma_{r_p}$ . Note that these fits are only valid for random pore radii that vary according to the specific distribution within the range of standard deviation values used for the fit. While the polynomials were fit using a specific average pore radius, they are valid for any average radius. Figure 9 shows  $E(r_p^{-4})$  from Monte Carlo simulations and calculated using Eq. (56) for the  $\bar{r}_p = 1 \mu\text{m}$  value used in the fit and for  $\bar{r}_p = 5 \text{ nm}$ , and in both cases, the equation is quite accurate. It is also clear that  $E(r_p^{-4})$  is sensitive to the standard deviation of the pore radius, with the sensitivity increasing with the value of the standard deviation.

As stated in the previous section, the impact of variation of the pore size on the expected value of the pinning force depends on whether  $f_c$  or  $N_p$  is considered to be deterministic. The same is true for the pore velocity. If we assume that  $N_p$  is deterministic, then  $f_c$  will vary, and the pore velocity becomes

$$v_p = P \frac{E(M_p)}{N_p}. \quad (59)$$

If we assume that the GB fractional coverage  $f_c$  is deterministic and the pore sizes vary, then  $N_p$  will also vary, and the pore velocity becomes

$$v_p = P E(M_p) E \left( \frac{1}{N_p} \right), \quad (60)$$

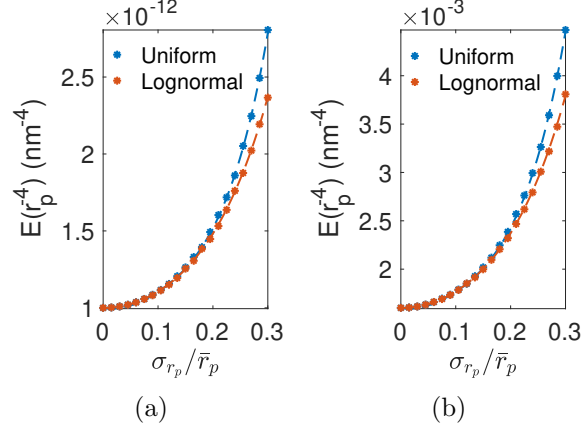


Figure 9: The expected value  $E(r_p^{-4})$  versus the ratio of the pore radius standard deviation to the mean for uniform and lognormal distributions, where (a) shows the values for the  $\bar{r}_p = 1 \mu\text{m}$  value used in the fit and (b) shows the values for  $\bar{r}_p = 5 \text{ nm}$ . Note that the fit is accurate for both average radii.

where  $E(1/N_p) = (\bar{r}_p^2 + \sigma_{r_p}^2)\pi/f_c$ .

### 2.4.3 Model of Grain Growth with Mobile Pores

Recent simulations of GB pinning by mobile porosity have shown that GB and pore interactions are complicated [54]. If the velocity of a pore and GB are equal, then both move forward together and stay in contact. However, if the velocity of the GB is faster than the pore, then the GB will wrap around the pore and may eventually release from it. One approach to modeling GB motion in the presence of mobile pores is to use an effective mobility that includes contributions from the mobilities of the GBs and the pores [56]. This approach assumes that the velocities of GBs and pores are equal and

$$\begin{aligned}
 v_p &= v_g, \\
 \frac{M_p}{N_p} P_g &= M_g (F_g - P_g), \\
 P_g \left( \frac{M_p}{N_p} + M_g \right) &= M_g F_g.
 \end{aligned} \tag{61}$$

If we substitute in  $P_g = v_p N_p / M_p$  and solve for  $v_g$ , we obtain

$$v_g = v_p = M_{eff} F_g, \tag{62}$$

where the effective mobility is given by

$$M_{eff} = \frac{M_g M_p}{M_p + N_p M_g}. \tag{63}$$

However, this approach forces the GBs and pores to have the same velocity and over-constrains the behavior when this is not the case.

We propose an alternative approach to modeling the GB velocity with mobile pores. In our new model, we begin with Eq. (33) but we consider mobile pores. In that case, the velocity from

Eq. (33) becomes the relative velocity of the GB with respect to the pores. If we consider  $P_g \leq F_g$  and use Eq. (53) to define the velocity of a pore, this gives

$$\begin{aligned} v_g - v_p &= M_g (F_g - P_g), \\ v_g &= M_g (F_g - P_g) + \frac{M_p}{N_p} P_g. \end{aligned} \quad (64)$$

We note that pores can slow a GB down, but they cannot speed one up. We therefore add the additional constraint

$$v_g = M_g F_g - \left[ M_g P_g - \frac{M_p}{N_p} P_g \right]^+. \quad (65)$$

Depending on the relative values of the GB and pore mobilities, and of the driving and resistive forces, this model suggests four different regimes:

1.  $M_g \leq \frac{M_p}{N_p}$  Pores are more mobile than GBs and so they have no impact on the GB velocity, irrespective of the resistive force. The second term in Eq. (65) is then null, leading to  $v_g = M_g F_g$ .
2.  $M_g \geq \frac{M_p}{N_p}$  and  $P_g < F_g$  Pores are slower than GBs and their resistive force is not enough to cancel out the driving force. The GB velocity is impacted by both the pore and GB mobilities, as defined by Eq. (65), though the  $\square^+$  operator is not needed.
3.  $M_g \gg \frac{M_p}{N_p}$  and  $P_g < F_g$  The pores are effectively immobile. Equation (65) becomes Eq. (33).
4.  $M_g \geq \frac{M_p}{N_p}$  and  $P_g \geq F_g$  The resistive force cancels out the driving force, so that GBs and pores migrate at the pore velocity. Eq. (65) becomes equal to Eq. (53), such that  $v_g = v_p = \frac{M_p}{N_p} F_g$ .

In the new model, if the variation of the pore size is considered, the equation is essentially unchanged, except that we calculate the expected grain velocity and we use the expected value of  $P_g$  in the first term in the  $\square^+$  operator,  $M_g P_g$  ( $M_g$  is deterministic). The expected value of the second term in the  $\square^+$  operator is given by

$$E \left( \frac{M_p}{N_p} P_g \right) = \frac{\gamma D_s \delta_s \Omega}{RT} E (r_p^{-3}). \quad (66)$$

The expected value  $E (r_p^{-3})$  also does not have a closed-form solution. We fit its value for the uniform and lognormal distributions in the same manner as was done for  $E (r_p^{-4})$ , with  $E (r_p^{-3}) = \bar{r}_p^{-3} p_3 \left( \frac{\bar{r}_p}{\sigma_{r_p}} \right)$ . The fitted values are given by

$$p_3^{uni} = 31.8a^3 - 1.9a^2 + 0.6a + 1.0, \quad (67)$$

$$p_3^{logn} = 10.9a^3 + 3.7a^2 + 0.2a + 1.0, \quad (68)$$

where  $a = \bar{r}_p / \sigma_{r_p}$ .

We demonstrate our model by calculating the velocity of a  $\text{UO}_2$  GB with a radius of curvature of  $7 \mu\text{m}$  at 1200 K. We use the GB energy and mobility defined by Eqs. (41) and (43), respectively, and the properties required to calculate the pore mobility are shown in Tab. 3. We consider two cases, one (shown in Figs. 10a and 10c) in which  $f_c = 0.05$  and we vary the pore average radius from 1 to 1000 nm ( $N_p$  decreases as the radius increases), and one (shown in Figs. 10b and 10d)

Property	Value	Reference
$D_s$	$D_{s0}e^{-\frac{E_m}{RT}}$	
$D_{s0}$	54 m <sup>2</sup> /s	[1]
$E_m$	452 kJ/mol	[1]
$\delta_s$	0.5 nm	<i>assumed</i>
$\Omega$	$M/\rho$	
$M$	270.03 g/mol	
$\rho$	10.97 g/cm <sup>3</sup>	

Table 3: Properties for UO<sub>2</sub> needed to calculate the pore mobility. The value or expression for each property is provided, as well as the reference when applicable.

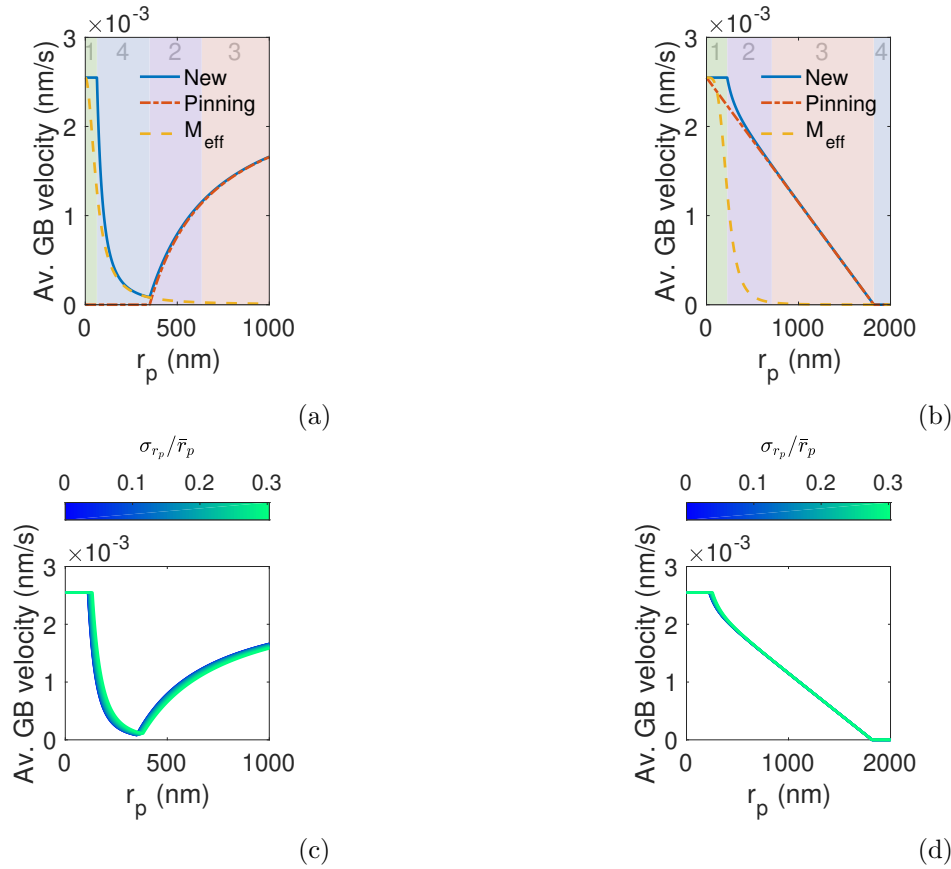


Figure 10: The velocity of a UO<sub>2</sub> GB with a radius of curvature  $R_g = 7 \mu\text{m}$  predicted by our new model (Eq. (65)) for various pore radii. (a) and (b) compare the value from the new model with that predicted by the  $M_{eff}$  (Eq. (62)) and the pinning model with static particles (Eq. (33)). The different regimes are shaded and labeled, where light green indicates Regime 1, light purple indicates Regime 2, light orange indicates Regime 3, and light blue indicates Regime 4. (c) and (d) demonstrate the impact of a lognormal pore size distribution, where the line colors indicate the ratio of the pore radius standard deviation to its mean. The cases shown in (a) and (c) have  $f_c = 0.05$  and the values of  $N_p$  changing with pore radius. The cases shown in (b) and (d) have  $N_p = 2.5 \times 10^{10}$  pores/m<sup>2</sup> and the value of  $f_c$  changing with radius.

in which  $N_p = 2.5 \times 10^{10}$  pores/m<sup>2</sup> and we vary the pore average radius from 1 to 2000 nm ( $f_c$  increases as the radius increases). We also calculate the velocity using the pinning model (Eq. (33)) and the effective mobility (Eq. (62)), for comparison.

The values of the average GB velocity for pore radii ranging from 1 to 1000 nm with the GB coverage  $f_c$  held constant are shown in Fig. 10a. The system is in Regime 1 for small values of the pore radius, as the mobility of small pores is very high. In Regime 1, our new model (Eq. (65)) predicts a velocity equal to the unimpeded GB velocity, since the pores are more mobile than the GB. The pinning model with static pores predicts that the GB is immobile (since  $P_g$  is a function of  $1/r_p$ , as shown in Eq. (48)), while the effective mobility predicts a velocity equal to the unimpeded velocity for the smallest pore but it decreases rapidly with increasing radius.

As the pore radius increases,  $\frac{M_p}{N_p}$  decreases and becomes smaller than  $M_g$  for  $r_p = 63$  nm, transitioning to Regime 4. In Regime 4, the new model predicts that the velocity rapidly decreases with increasing radius, and its prediction is roughly equivalent to the effective mobility. The pinning model still predicts that the GB is immobile.

Like  $M_p$ ,  $P_g$  also decreases with increasing pore radius (though it changes with  $1/r_p$  rather than  $1/r_p^4$ , like  $M_p$ ); once  $r_p > 350$  nm,  $P_g < F_g$  and the system is in Regime 2. The new model predicts that the GB velocity now increases with increasing radius, due to the decrease in  $P_g$ . The pinning model also predicts an increasing GB velocity with increasing radius, and its predicted velocity is slightly slower than that from the new model. The effective mobility predicts that the velocity continues to decrease with increasing radius.

As both  $M_p$  and  $P_g$  continue to decrease, the pores become effectively immobile and the system enters Regime 3 around  $r_p = 640$  nm. The new model and the pinning model predictions are identical, predicting that the GB velocity increases with increasing pore radius, but at a decreasing rate. The velocity from the effective mobility is essentially zero.

GBs impeded by mobile pores should move at velocities equal to or faster than GBs impeded by immobile particles/pores. Our new model predicts velocities much faster than the pinning model in Regimes 1 and 4, slightly faster than the pinning model in Regime 2, and equal to the pinning model in Regime 3. The effective mobility also predicts GB velocities that are faster than the pinning model in Regimes 1 and 4, but it predicts velocities that are much slower than the pinning model in Regimes 2 and 3.

The values of average GB velocity for pore radii ranging from 1 to 2000 nm when the number of pores per unit GB area  $N_p$  is held constant are shown in Fig. 10b. The system is again in Regime 1 for small values of the pore radius, and our new model again predicts a velocity equal to the unimpeded GB velocity. With  $N_p$  constant, the pinning model predicts the unimpeded GB velocity for  $r_p = 1$  nm, and it decreases linearly with  $r_p$ , since  $P_g$  is now a linear function of  $r_p$ , as shown in Eq. (49). The effective mobility predicts a velocity higher than the pinning model for very small pore radii, but its velocity decreases quickly with increasing pore radius and drops below the pinning model.

The pore velocity decreases rapidly with increasing pore radius, and the system enters Regime 2 as  $M_p/N_p$  decreases and becomes smaller than  $M_g$  at  $r_p = 225$  nm. In Regime 2, our new model decreases rapidly with increasing radius and approaches the velocity predicted by the pinning model. The effective mobility predicts a GB velocity that is much lower than the pinning model.

When  $r_p > 710$  nm, the pores are effectively immobile. Here, the system enters Regime 3, in which the new and pinning models are equivalent. The velocity from the effective mobility is effectively zero for all  $r_p > 710$  nm.

At  $r_p = 1818$  nm, the system enters Regime 4 with  $F_g = P_g$  and  $M_p \approx 0$ , such that all three models predict that the GBs are immobile.

From the results of these two cases, it is clear that our new model accounts for the correct



physics in each of the four regimes. The pinning model tends to under-predict the GB velocity in regimes 1, 2, and 4, since it assumes immobile pores. The effective mobility tends to under-predict the GB velocity in regimes 1, 2, and 3, since it forces the GB and pore velocities to be equal.

The impact of variation in the pore size differs between the two cases because the pore radius standard deviation affects  $P_g$  differently in each. We demonstrate the impact of variation in the pore size by modeling the same two cases but now allowing the pore size to vary according to a lognormal distribution. The simulations are repeated for values of the ratio of the pore radius standard deviation to its mean ranging from 0 to 0.3.

When  $f_c$  is held constant (Fig. 10c), both  $P_g$  and  $M_p$  increase as the standard deviation increases. The standard deviation has no impact on the GB velocity in Regime 1, because the pores are too mobile to impact the GB migration. In Regime 4, the GB velocity increases as the standard deviation increases for a given average pore radius, since the velocity is dominated by the pore mobility. The GB velocity decreases as the standard deviation increases for a given average pore radius in Regimes 2 and 3, since the velocity is dominated by the resistive force. The radii at which the system transitions between the various regimes increases as the standard deviation increases.

When  $N_p$  is held constant (Fig. 10d), only  $M_p$  increases as the standard deviation increases, and  $P_g$  is independent of the standard deviation. Again, the GB velocity is independent of the standard deviation in Regime 1. In Regime 2, the velocity increases with increasing standard deviation due to the increase in  $M_p$ . The velocity is unchanged by the standard deviation in Regimes 3 and 4. The radius at which the system transitions between Regimes 1 and 2 increases as the standard deviation increases, but all the other transitions are independent of the standard deviation.

While the impact of variation in the pore size on the GB velocity is significant, as illustrated by Figs. 10c and 10d, it is small compared to the impact of the pore radius. A pore size distribution will not result in large changes to the grain growth of a material.

Equation (65) describes the velocity of a specific GB. If we consider a polycrystal with average grain size  $\bar{D}$  with only the curvature driving force, as we did to develop Eq. (35), but we let the change in the average velocity be described by Eq. (65), we obtain:

$$\frac{\partial \bar{D}}{\partial t} = \alpha \bar{M} \frac{\bar{\gamma}}{\bar{D}} - \alpha^{\frac{1}{2}} \left[ \bar{M} \bar{P} - \frac{M_p}{N_g} \bar{P} \right]^+. \quad (69)$$

Given the initial average grain size  $\bar{D}_0$ , this equation can be solved numerically to determine the average grain size as a function of time. It can be applied to any material with pores resisting grain growth for which curvature is the only significant driving force and for which the pore mobility and the GB mobility and energy are known.

#### 2.4.4 Grain Growth Model for $\text{UO}_2$

The new mechanistic grain growth model must predict the change in the average grain size of  $\text{UO}_2$  as a function of temperature, the sintered porosity  $p$  and their average radius, and the fission gas bubbles defined by the fraction of GBs covered by fission gas  $f_c$  and their average radius. These variables describing the average state of the fuel microstructure at a given material point would be calculated by a densification model for  $p$  and a fission gas release model for  $f_c$ . The model from Eq. (69) defines the change in the average grain size in a microstructure with pores, but it only considers one type of pore. The model needs to be expanded to consider the impact of two types of pores, namely the sintered pores and the fission gas bubbles.

If both types of porosity are more mobile than the GBs, then the pores have no impact on the grain growth. If only one type of porosity is more mobile than the GBs, then the other impacts

the change in the average grain size with time according to Eq. (69). If both types of porosity are less mobile than the GBs, then both types of porosity will impact the grain growth. If the sum of the two resistive pressures is greater than or equal to the driving force, then the GBs are fully pinned and they move with the mobility of the pores. However, since the mobility of the two types of pores will vary, we use an effective pore mobility, such that

$$\frac{\partial \bar{D}}{\partial t} = \alpha M_{p,eff} \frac{\bar{\gamma}}{\bar{D}}. \quad (70)$$

The effective pore mobility is given by

$$M_{p,eff} = \frac{\sum_i f_{c,i} M_{p,i} / N_{p,i}}{\sum_i f_{c,i}}, \quad (71)$$

where  $f_{c,i}$ ,  $M_{p,i}$ , and  $N_{p,i}$  are the fractional coverage, pore mobility, and number of pores per unit GB area of the porosity type  $i$ , respectively. If the GBs are not fully pinned, the average grain size changes according to

$$\frac{\partial \bar{D}}{\partial t} = \alpha \bar{M} \frac{\bar{\gamma}}{\bar{D}} - \alpha^{\frac{1}{2}} \sum_p \left[ \bar{M} \bar{P}_i - \frac{M_{p,i}}{N_{p,i}} \bar{P}_i \right]^+, \quad (72)$$

where  $\bar{P}_i$  is the average resistive force of porosity type  $i$ , and the sum is taken over the two types of porosity: sintered pores and fission gas bubbles.

## 2.5 Model Validation

We have validated the mechanistic grain growth model presented in the previous section using two validation cases, one on unirradiated  $\text{UO}_2$  and one on irradiated  $\text{UO}_2$ .

### 2.5.1 Grain growth in unirradiated $\text{UO}_2$

For the first validation case, we compared against grain growth data in unirradiated  $\text{UO}_2$  samples from Ainscough et al. [7]. As discussed above, these samples have porosity left over from sintering that resist grain growth and can be accounted for with our new model. While Ainscough et al. provide grain growth data from twelve different batches, we selected three to compare against: Batches 3, 7, and 12. We selected these batches because they are the only batches with data quantifying the densification of the fuel during the experiment, though only the initial and final densities are provided. The authors state that the densification is not linear and that in many cases it ceased after the first third of the annealing time, but no specific information is given about the individual batches. Also, no information was provided regarding the sizes of the pores.

We applied our model to simulate the increase in the average grain size of Batches 3, 7, and 12 at 1400°C and 1500°C using the properties from Tab. 3 as well as the GB energy and mobility from Eqs. (41) and (43). We assumed that the pore volume fraction decreased due to densification according to  $\dot{f}_V = -A f_V^{1/3}$ , as suggested by the model from Kang et al. [72]. We determined the value for  $A$  using the given initial and final relative densities. We also assumed that the average pore radius was different in the different batches, and that the pore radii followed a lognormal distribution with a standard deviation  $\sigma_{r_p} = 0.2 \bar{r}_p$ . We fitted the values of the average radii by minimizing the error for the 1400°C case and used the 1500°C case for validation. The fitted  $\bar{r}_p$  were 7.5  $\mu\text{m}$  for Batch 3, 4.3  $\mu\text{m}$  for Batch 7, and 2.3  $\mu\text{m}$  for Batch 12. Note that the fit values for the average pore radii increased with average grain size.

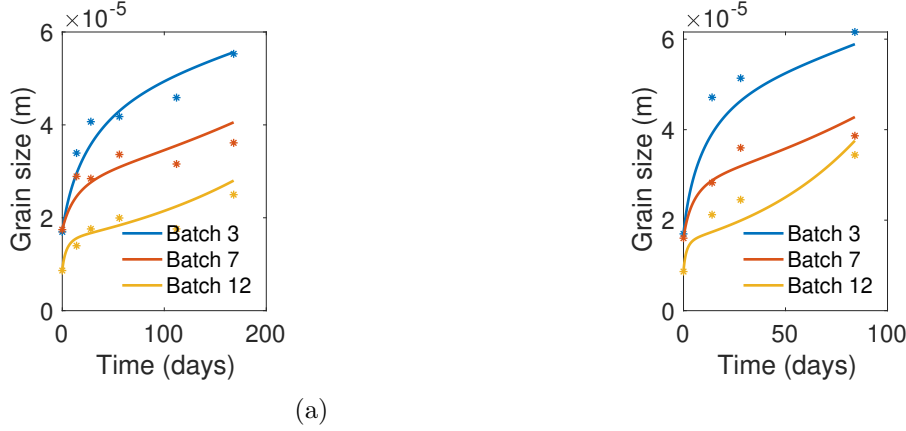


Figure 11: Validation of our new grain growth model by comparing to grain growth data for unirradiated  $\text{UO}_2$  [7]. Specifically, we compare against data from Batches 3, 7, and 12. The average pore radii were fit using the data at 1400°C, shown in (a), and we validated the model using the data at 1500°C, shown in (b).

The predicted average grain sizes at 1400°C after fitting  $\bar{r}_p$ , as well as the experimental data, are shown in Fig. 11a. The predicted average grain sizes and the experimental data at 1500°C are shown in Fig. 11b, and they compare reasonably well with the experimental data. For Batch 3, the predicted average grain sizes are somewhat below the experimental grain sizes; for Batch 7, they compare well; for Batch 12, they are below the experimental grain sizes initially but the final average grain size is slightly above the experimental value. Thus, the model performs well for fresh fuel. Note that the pore mobility is negligible for these cases due to the large average pore radii, such that the growth is only a function of the GB energy and mobility, and the pinning force.

### 2.5.2 Grain growth in irradiated $\text{UO}_2$

Next, we validated against grain growth data from irradiated fuel. In irradiated fuel, the porosity left over from sintering resists grain growth. However, the volume fraction of sintered porosity decreases with time due to irradiation-enhanced densification. In addition, gaseous fission products segregate to GBs and form bubbles that resist grain growth. Ainscough et al. [7] provide grain growth data from two irradiated fuel pellets, each irradiated at a different power and for a different time. Little information is given about how the data were collected, but it appears that the average grain size was measured at various locations across the radius of the pellets during post-irradiation examination. These average grain sizes were then correlated with corresponding irradiation temperatures, which must have been calculated using a model, since the capability to measure the temperature at multiple locations across the radius of a fuel pellet within a reactor was not available in 1973 (and would be difficult even today). The final burnups of the specimens were given, but no data regarding their sintered porosity or the fission gas bubble contents were provided.

Since these data do not provide any information regarding the porosity in the fuel microstructure, we cannot use our new model to predict the grain growth and directly compare it with the data. However, Ainscough et al. used these data to fit a burnup-dependent empirical model for the maximum grain size from Eq. (38). This empirical grain growth model is currently used in the BISON fuel performance code [73], along with an empirical densification model that decreases

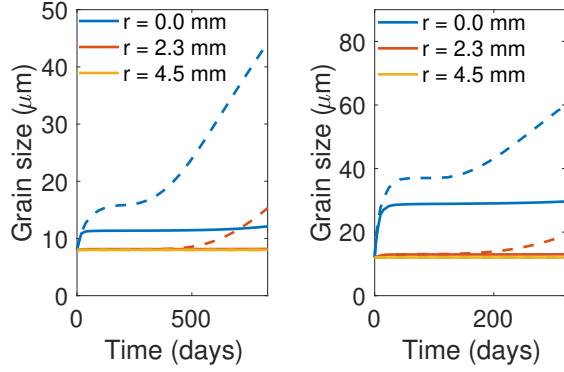
the sintered porosity over time, and a fission gas release model that evolves descriptions of the GB fission gas bubbles. These models in BISON provide a means of estimating the porosity evolution within irradiated fuel and the prediction of the empirical grain growth model can be used as a rough surrogate for experimental data. Thus, we used values of the temperature, sintered porosity behavior, and fission gas bubble behavior outputted from BISON simulations in our model and predicted the increase in the average grain size. We then compared these predictions against the empirical grain growth model developed by Ainscough et al. [7].

We ran two BISON simulations and outputted the temperature, volume fraction of sintered porosity, GB fractional coverage by fission gas bubbles, and average GB bubble radius at various locations. The BISON simulations predicted the fuel performance of a smeared ten pellet rodlet in axisymmetric coordinates (as described in Ref. [73] and using a standard example input file). One simulation was carried out at a linear power of 29 kW/m for 830 days and the other at a linear power of 37 kW/m for 320 days. For each, the values were outputted at the pellet center ( $r = 0$  mm), at an intermediate radius ( $r = 2.3$  mm), and near the outer radius ( $r = 4.5$  mm). The 29 kW/m and 37 kW/m cases were conducted with initial average grain sizes of 8  $\mu\text{m}$  and 12  $\mu\text{m}$ , respectively. The densification model in BISON does not determine the average radius of the sintered porosity, so we used the fitted value of 2.3  $\mu\text{m}$  from the previous example from the batch with the closest initial grain size (Batch 3). We also assumed that the size of all porosity varied according to a lognormal distribution with  $\sigma_{r_p} = 0.2\bar{r}_p$ . We calculated the average grain size over time using our new model and compared its predictions with those from the empirical grain growth model from Ref. [7]. We used the properties from Tab. 3 and Eqs. (41) and (43).

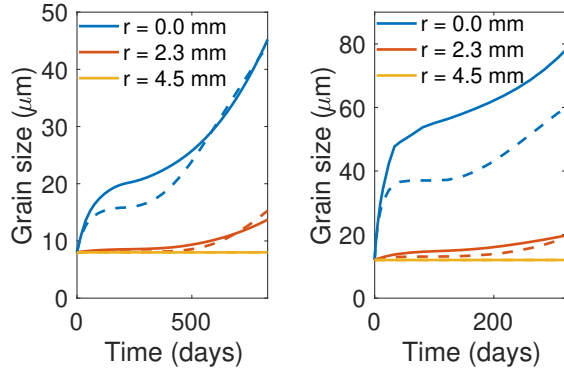
When we used all the values from Tab. 3 in our model, it predicted much less grain growth than the empirical model, as shown in Fig. 12a. Both the models predict no grain growth at the outer edge of the fuel ( $r = 4.5$  mm). At mid-radius ( $r = 2.3$  mm), the empirical model predicted significant growth starting halfway through the irradiation time for both powers, but the new model predicted no growth for the 29 kW/m case and small initial growth for the 37 kW/m case. At the pellet center ( $r = 0.0$  mm), the empirical model predicted rapid initial growth, then a region of no growth, and then a long region of linear growth while the new model only predicted rapid initial growth and no additional growth. One likely reason for this discrepancy is inaccuracy in the surface diffusivity. We obtained the activation energy  $E_m$  and prefactor  $D_{s0}$  for the surface diffusivity from Maiya [1], and in that work, they report an uncertainty of 10% to 15% on the activation energy. In addition, it is well known that the high concentration of vacancies that occurs during irradiation will accelerate diffusion.

To improve the performance of the model, we calibrated the value of the activation energy for surface diffusion using the 29 kW/m case. We found that a value of  $E_m = 389$  kJ/mol gave the best performance, a 13.9% variation from the value reported by Maiya [1] and within the reported 10% to 15% uncertainty. The simulation predictions using the calibrated activation energy are shown in Fig. 12b. After calibration against the 29 kW/m case, our new model predicted grain growth very similar to that from the empirical model. However, the final grain size is under-predicted at mid-radius and the grain size in the first half of the irradiation at the center is over-predicted. Using the calibrated value with the 37 kW/m case, the new model over-predicted the grain size at both mid-radius and at the pellet center, though the general trends are captured. At mid-radius, the final grain sizes compared very well. At the pellet center, our new model over-predicted the final grain size.

Though this validation is far from ideal because we are using descriptions of the porosity from models in BISON and we are comparing the grain sizes to an empirical model rather than experimental data, the comparison is reasonable for the 37 kW/m case, for which no calibration was carried out. Thus, we now have a mechanistic model that predicts the change in the average grain



(a)



(b)

Figure 12: Comparison of the grain sizes from our grain growth model to those predicted by the empirical model using values taken from BISON simulations. Results using a linear power of 29 kW/m are on the left and using a linear power of 37 kW/m are on the right. (a) shows the results using the published surface diffusion activation energy, and (b) shows the results using the activation energy that was calibrated using the 29 kW/m result. In each figure, solid lines show results from our new model, and dashed lines show results from the empirical model [7].

size as a function of the temperature and porosity in the fuel. It can also be applied to other reactor fuels, as long as curvature is the only significant driving force, and the fission gas bubble mobility and GB mobility and energy are known.

## 2.6 Impact on Fuel Performance Simulations

Having validated the model against experimental sintering data and an empirical grain growth model, we now show its impact on the results of fuel performance simulations. Our mechanistic grain growth model has been implemented in the BISON fuel performance tool [73]. It includes the impact of sintered porosity that decreases due to densification and fission gas bubbles that increase during reactor operation in the same manner as was done in Sec. 2.5.2. However, now the grain growth model is fully integrated into the BISON simulation, and the evolving grain size at every integration point in the mesh directly impacts the fission gas release model as part of the mechanistic set of materials models [74].

To demonstrate the performance of the new grain growth model in BISON, we incorporated it

into one of the BISON assessment cases: Rod TSQ002 from the US PWR  $16 \times 16$  assessment [75]. However, in the standard assessment case the power was low enough that the fuel temperature never exceeded 1250 K and very little grain growth would have occurred. To provide cases that clearly demonstrate the capabilities of our new model, we changed the average linear heat rate to result in higher temperatures and substantial grain growth. We modeled two modified versions of the assessment. In the first, the average linear heat rate is constant with time; in the second, the relative changes with time in the average linear heat rate are unchanged from the original assessment but its magnitude is increased. These changes to the average linear heat rate make it impossible to make comparisons to other published results for this assessment case, but they provide a useful means of assessing the impact of our new grain growth model on the overall fuel performance, as compared to BISON simulations using the empirical model from Ainscough et al. [7]. In particular, the transient power case emphasizes the importance of including the impact of temperature and power history on grain growth, which is included in mechanistic models, like our new model, but not in empirical models. The fuel had an initial grain size of  $17.6 \mu\text{m}$ . The simulations used the fitted value for  $E_m$ , the other values from Tab. 3, and Eqs. (41) and (43).

We first discuss the results from the simulations with constant power. The average linear heat rate used in the simulations is shown in Fig. 13a. The average grain size was outputted at an axial position approximately halfway up the rod (2 m) at three radial locations ( $r = 0$  mm, 2 mm, and 4 mm). The temperatures at those locations are shown in Fig. 13c, and the grain sizes are shown in Fig. 13d.

The temperature at the outer edge of the fuel pellet was cool enough that no grain growth occurred. At mid-radius (2 mm), our new grain growth model predicted significant grain growth starting after 2.5 years, reaching a final grain size of  $20.4 \mu\text{m}$  after 4.5 years. The empirical model did not predict any significant grain growth until 4.0 years. However, once it started, it was much faster than predicted by the new model and the final grain size was  $19.6 \mu\text{m}$ . At the center of the pellet, our new grain growth model again predicted the start of grain growth much earlier than the empirical model, but the final grain size predicted by the two models was quite similar ( $39.8 \mu\text{m}$  from our new model and  $41.3 \mu\text{m}$  from the empirical model). After about 4 years, the predicted grain growth at the pellet center from the two models converged and from then on they were nearly identical.

A sensitivity study carried out on the fission gas release model in BISON [45] showed that the predicted fission gas release is somewhat sensitive to grain size, while the predicted gaseous swelling is highly sensitive to grain size. Therefore, we compare the fractional fission gas release and the gaseous swelling in the two simulations. The fission gas release fraction is shown in Fig. 13e. While there is some deviation between the two simulations, especially at around 3 years, it is not large, and after 4.5 years there is almost no deviation. This indicates that the differences in the predicted grain size do not have a significant impact on the fission gas release. We see a similar trend in the gaseous swelling, shown in Fig. 13f. There is almost no deviation at the pellet edge and mid-radius, though at the pellet center the swelling is slightly larger in the simulation using our new model after about 3 years.

The average linear heat rate used for the transient case is shown in Fig. 13b, and the resultant temperatures at the same radial locations used for the constant power case are shown in Fig. 13g. For this case, the new grain growth model predicted significantly more grain growth at mid-radius and at the center of the fuel pellet than the empirical model. However, the empirical model was fit to constant power data and is independent of the temperature history of the material, i.e. it will predict the same change in grain size at a given temperature and burnup whether the material was at a higher temperature previously or whether the temperature has been constant. In reality, the temperature history will impact the evolution of the sintered porosity and fission gas bubbles

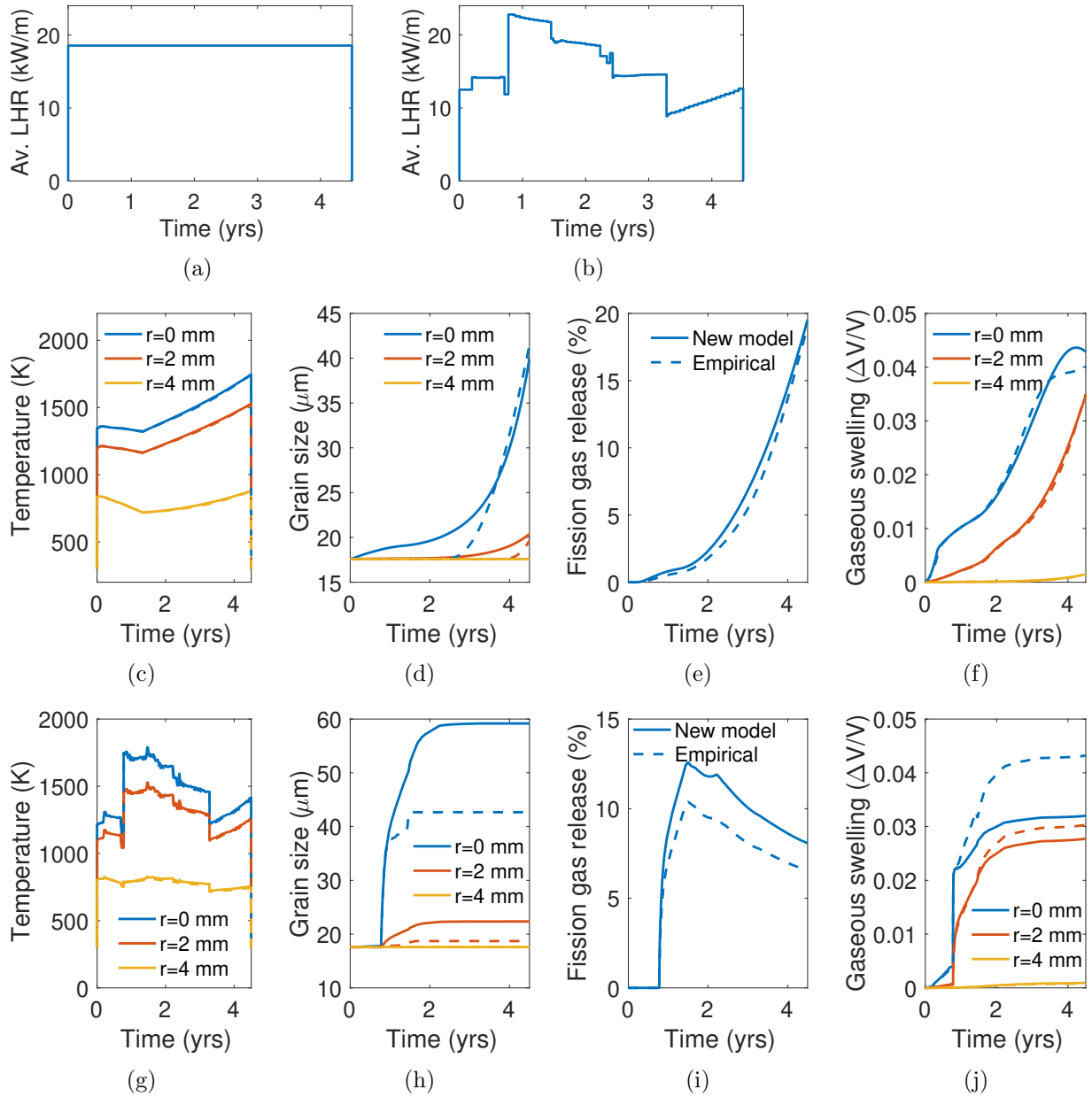


Figure 13: Impact of our grain growth model on fuel performance simulations using BISON for constant and transient power cases. (a) and (b) show the average linear heat rates for the two cases. (c) - (f) show results for the constant power case, and (g) - (j) show results for the transient power case. (c) and (g) show the pellet temperature with time at three radial locations at an axial location of 2 m (approximately mid-rod), (d) and (h) show the grain size with time at the same radial and axial locations, (e) and (i) show the fractional fission gas release with time, and (f) and (j) show the gaseous swelling at the same locations. In each figure, solid lines show results obtained using the new grain growth model and dashed lines show results obtained using the empirical model from Ainscough et al. [7].

in the material and therefore will impact grain growth. The grain growth predicted by our new mechanistic model is directly a function of the evolution predicted by the densification and fission gas release models and therefore does account for this history effect. It predicts more grain growth than the empirical model because the high temperatures in the first few years of the irradiation reduced the resistive force due to the bubbles and porosity.

The significant grain growth that occurs during the high temperature transients in this case results in an increase in fission gas release and a decrease in gaseous swelling, as compared to the results with the empirical model. The increase in fission gas release begins at the start of the first transient (after 1 year), and the fractional release in the simulations using our new model is higher than that using the empirical model for the rest of the simulation (with a final difference of 20%). Note that the fractional release decreases after about two years because as the temperature decreases, fission gas diffusion is slowing at a much higher rate than the decrease in gas production, trapping more gas within the fuel. The gaseous swelling at the outer radius of the pellet is the same in both simulations; at the mid-radius, the simulation using our new model results in less swelling than that using the empirical model after about two years with a final difference of about 10%. At the pellet center, the simulation using our new model results in less swelling starting after about one year, with a final difference of 35%. It is important to note that the fission gas release model in BISON [44] is a mechanistic model and does correctly consider the impact of the temperature and power history; therefore, these differences fully result from our new grain growth model. Thus, the fact that the empirical grain growth model does not consider the impact of power transients can significantly increase the error in the prediction of fission gas release and gaseous swelling.

## 2.7 Conclusions and Future Work

We have developed a mechanistic grain growth model for  $\text{UO}_2$  that accounts for pinning by porosity left over from sintering and by fission gas bubbles, and that accounts for dragging of porosity by GBs. In support of the model, we have created a new fit (including uncertainty limits) of existing experimental data to obtain the average GB energy as a linear function of temperature, which is also consistent with atomistic simulation results. We used this fit along with data presented in Ainscough et al. [7] to create a new fit of the average GB mobility and its associated uncertainty limits. Our results indicate that recent data from nanocrystalline  $\text{UO}_2$  samples [8] likely have an additional driving force, such as residual stress, that causes them to differ from the older data.

We have presented a model of the resistive force due to particles/pores that considers either a uniform or lognormal particle/pore size distribution. We have also developed a model of the pore mobility that considers a pore size distribution. We then developed a model of grain growth with mobile pores and compared its predictions to the classical pinning and effective mobility models. Our new model that considers mobile pores accurately describes the behavior of four different regimes related to the relationships between the GB and pore mobilities and the driving and resistive forces. The pinning and effective mobility models each only accurately describe the GB velocity for one of the four regimes. We then expanded the model to include two distributions of porosity: sintered porosity and fission gas bubbles. The model was then calibrated to and validated against grain growth data for unirradiated  $\text{UO}_2$  and the empirical grain growth model for irradiated  $\text{UO}_2$  from Ainscough et al. [7]. Finally, we demonstrated the impact of our new mechanistic model on fuel performance simulations using the BISON tool for constant and transient power cases. Our model predicts similar results to the empirical model for the constant power case. However, since the new mechanistic model accounts for the impact of the temperature and power history on fuel microstructure, it predicts significantly more grain growth for the transient power case. While the mechanistic model was presented here for  $\text{UO}_2$ , it could be used for other fuels in which curvature



is the only significant driving force, as long as the pore mobility and GB mobility and energy are known or can be estimated.

In future work, the mechanistic model presented here will be adapted to doped  $\text{UO}_2$  fuel. A mechanistic model for densification in doped  $\text{UO}_2$  fuel will be developed and coupled to the grain growth model presented in this Section, and its impact on fuel performance simulations will be evaluated as described here.

### 3 References

1. P. S. Maiya. Surface diffusion, surface free energy, and grain-boundary free energy of uranium dioxide. *Journal of Nuclear Materials*, 40(1):57–65, July 1971.
2. E. N. Hodkin and M. G. Nicholas. Surface and interfacial properties of stoichiometric uranium dioxide. *Journal of Nuclear Materials*, 47(1):23–30, May 1973.
3. E. N. Hodkin and M. G. Nicholas. Surface and interfacial properties of non-stoichiometric uranium dioxide. *Journal of Nuclear Materials*, 67(1):171–180, June 1977.
4. P. Nikolopoulos, S. Nazaré, and F. Thümmeler. Surface, grain boundary and interfacial energies in  $\text{UO}_2$  and  $\text{UO}_2\text{-Ni}$ . *Journal of Nuclear Materials*, 71(1):89–94, December 1977.
5. Pankaj V. Nerikar, Karin Rudman, Tapan G. Desai, Darrin Byler, Cetin Unal, Kenneth J. McClellan, Simon R. Phillpot, Susan B. Sinnott, Pedro Peralta, Blas P. Uberuaga, and Christopher R. Stanek. Grain Boundaries in Uranium Dioxide: Scanning Electron Microscopy Experiments and Atomistic Simulations. *Journal of the American Ceramic Society*, 94(6):1893–1900, June 2011.
6. Timothy Harbison. *Anisotropic grain boundary energy function for uranium dioxide*. PhD thesis, Brigham Young University-Idaho, 2015.
7. J. B. Ainscough, B. W. Oldfield, and J. O. Ware. Isothermal grain growth kinetics in sintered  $\text{UO}_2$  pellets. *Journal of Nuclear Materials*, 49(2):117–128, December 1973.
8. Tiankai Yao, Kun Mo, Di Yun, Sonal Nanda, Abedellatif M. Yacout, and Jie Lian. Grain growth and pore coarsening in dense nano-crystalline  $\text{UO}_2\text{+x}$  fuel pellets. *Journal of the American Ceramic Society*, 100(6):2651–2658, 2017.
9. J. T. White, A. T. Nelson, J. T. Dunwoody, D. D. Byler, D. J. Safarik, and K. J. McClellan. Thermophysical properties of  $\text{U}_3\text{Si}_2$  to 1773 K. *Journal of Nuclear Materials*, 464:275–280, 2015.
10. Y. B. Miao, K. A. Gamble, D. Andersson, B. Ye, Z. G. Mei, G. Hofman, and A. M. Yacout. Gaseous swelling of  $\text{U}_3\text{Si}_2$  during steady-state LWR operation: A rate theory investigation. *Nuclear Engineering and Design*, 322:336–344, 2017.
11. Y. B. Miao, K. A. Gamble, D. Andersson, Z. G. Mei, and A. M. Yacout. Rate theory scenarios study on fission gas behavior of  $\text{U}_3\text{Si}_2$  under LOCA conditions in LWRs. *Nuclear Engineering and Design*, 326:371–382, 2018.
12. M. R. Finlay, G. L. Hofman, and J. L. Snelgrove. Irradiation behaviour of uranium silicide compounds. *Journal of Nuclear Materials*, 325:118–128, 2004.
13. Y. B. Miao, J. Harp, K. Mo, S. Bhattacharya, P. Baldo, and A. M. Yacout. Short communication on "in-situ TEM ion irradiation investigations on  $\text{U}_3\text{Si}_2$  at LWR temperatures". *Journal of Nuclear Materials*, 484:168–173, 2017.
14. Y. B. Miao, J. Harp, K. Mo, S. F. Zhu, T. K. Yao, J. Lian, and A. M. Yacout. Bubble morphology in  $\text{U}_3\text{Si}_2$  implanted by high-energy Xe ions at 300 degrees C. *Journal of Nuclear Materials*, 495:146–153, 2017.

15. Y. B. Miao, J. Harp, K. Mo, Y. S. Kim, S. F. Zhu, and A. M. Yacout. Microstructure investigations of  $\text{U}_3\text{Si}_2$  implanted by high-energy Xe ions at 600 degrees C. *Journal of Nuclear Materials*, 503:314–322, 2018.
16. T. K. Yao, B. W. Gong, L. F. He, J. Harp, M. Tonks, and J. Lian. Radiation-induced grain subdivision and bubble formation in  $\text{U}_3\text{Si}_2$  at LWR temperature. *Journal of Nuclear Materials*, 498:169–175, 2018.
17. T. K. Yao, B. W. Gong, L. F. He, Y. B. Miao, J. M. Harp, M. Tonks, and J. Lian. In-situ TEM study of the ion irradiation behavior of  $\text{U}_3\text{Si}_2$  and  $\text{U}_3\text{Si}_5$ . *Journal of Nuclear Materials*, 511:56–63, 2018.
18. H. Shimizu. The properties and irradiation behavior of  $\text{U}_3\text{Si}_2$ . Technical Report NAA-SR-10621, Atomics International, 1965.
19. J. Rest. A model for fission-gas-bubble behavior in amorphous uranium silicide compounds. *Journal of Nuclear Materials*, 325(2-3):107–117, 2004.
20. T. Barani, G. Pastore, D. Pizzocri, D. A. Andersson, C. Matthews, A. Alfonsi, K. A. Gamble, P. Van Uffelen, L. Luzzi, and J. D. Hales. Multiscale modeling of fission gas behavior in  $\text{U}_3\text{Si}_2$  under LWR conditions. *Journal of Nuclear Materials*, 522:97–110, 2019.
21. G. Pastore, L. Luzzi, V. Di Marcello, and P. Van Uffelen. Physics-based modelling of fission gas swelling and release in  $\text{UO}_2$  applied to integral fuel rod analysis. *Nucl. Engrg. Design*, 256:75–86, 2013.
22. B. Beeler, M. Baskes, D. Andersson, M. W. D. Cooper, and Y. F. Zhang. Molecular dynamics investigation of grain boundaries and surfaces in  $\text{U}_3\text{Si}_2$ . *Journal of Nuclear Materials*, 514:290–298, 2019.
23. L. K. Aagesen, D. Schwen, M. R. Tonks, and Y. F. Zhang. Phase-field modeling of fission gas bubble growth on grain boundaries and triple junctions in  $\text{UO}_2$  nuclear fuel. *Computational Materials Science*, 161:35–45, 2019.
24. R.J.White. The development of grain-face porosity in irradiated oxide fuel. *Journal of Nuclear Materials*, 325:61–77, 2004.
25. G. Pastore, L.P. Swiler, J.D. Hales, S.R. Novascone, D.M. Perez, B.W. Spencer, L. Luzzi, P. Van Uffelen, and R.L. Williamson. Uncertainty and sensitivity analysis of fission gas behavior in engineering - scale fuel modeling. *Journal of Nuclear Materials*, 456:398–408, 2015.
26. T. Kogai. Modelling of fission gas release and gaseous swelling of light water reactor fuels. *Journal of Nuclear Materials*, 244:131–140, 1997.
27. P. C. Millett, M. R. Tonks, S. B. Biner, L. Z. Zhang, K. Chockalingam, and Y. F. Zhang. Phase-field simulation of intergranular bubble growth and percolation in bicrystals. *Journal of Nuclear Materials*, 425(1-3):130–135, 2012.
28. M. R. Tonks, D. Gaston, P. C. Millett, D. Andrs, and P. Talbot. An object-oriented finite element framework for multiphysics phase field simulations. *Computational Materials Science*, 51:20–29, 2012.

29. D.R.Olander. *Fundamental aspects of nuclear reactor fuel elements*. Technical Information Center, Energy Research and Development Administration, 1976.
30. N. Moelans. A quantitative and thermodynamically consistent phase-field interpolation function for multi-phase systems. *Acta Materialia*, 59(3):1077–1086, 2011.
31. D. A. Andersson, X. Y. Liu, B. Beeler, S. C. Middleburgh, A. Claisse, and C. R. Stanek. Density functional theory calculations of self- and Xe diffusion in  $\text{U}_3\text{Si}_2$ . *Journal of Nuclear Materials*, 515:312–325, 2019.
32. Yulan Li, Shenyang Hu, Robert Montgomery, Fei Gao, and Xin Sun. Phase-field simulations of intragranular fission gas bubble evolution in  $\text{UO}_2$  under post-irradiation thermal annealing. *Nuclear Instruments and Methods in Physics Research Section B: Beam Interactions with Materials and Atoms*, 303:62–67, 2013.
33. C. Kittel and H. Kroemer. *Thermal Physics*. W. H. Freeman and Company, 1980.
34. N. Moelans, B. Blanpain, and P. Wollants. Quantitative analysis of grain boundary properties in a generalized phase field model for grain growth in anisotropic systems. *Phys. Rev. B*, 78:024113, 2008.
35. <http://nele.studentenweb.org/docs/parameters.m>; accessed 07-Oct-2017.
36. International Atomic Energy Agency. Chain fission yields. <https://www-nds.iaea.org/sgnucdat/c1.htm>; accessed 13-Apr-2017.
37. M. Plapp. Unified derivation of phase-field models for alloy solidification from a grand-potential functional. *Physical Review E*, 84(3):031601, 2011.
38. M. W. D. Cooper, C. Matthews, C. R. Stanek, D. A. Andersson, K. Gamble, B. W. Beeler, and G. Pastore. Fission gas and creep in uranium silicide fuel. Report L3:FMC.FUEL.P19.05, Los Alamos National Laboratory, 2019.
39. D. Gaston, C. Newman, G. Hansen, and D. Lebrun-Grandié. MOOSE: A parallel computational framework for coupled systems of nonlinear equations. *Nuclear Engineering and Design*, 239:1768–1778, 2009.
40. J. D. Hales, K. A. Gamble, B. W. Spencer, S. R. Novascone, G. Pastore, W. Liu, D. S. Stafford, R. L. Williamson, D. M. Perez, and R. J. Gardner. BISON users manual. Technical Report INL/MIS-13-30307, Rev. 3, Idaho National Laboratory, September 2015.
41. J. K. Mason, E. A. Lazar, R. D. MacPherson, and D. J. Srolovitz. Geometric and topological properties of the canonical grain-growth microstructure. *Physical Review E*, 92(6), 2015.
42. B. Lorenz, I. Orgzall, and H.-O. Heuer. Universality and cluster structures in continuum models of percolation with two different radius distributions. *Journal of Physics A: Mathematical and General*, 26:4711–4722, 1993.
43. V. E. Brunini, C. A. Schuh, and W. C. Carter. Percolation of diffusionally evolved two-phase systems. *Physical Review E*, 83:021119, 2011.
44. Giovanni Pastore, Lelio Luzzi, Valentino Di Marcello, and Paul Van Uffelen. Physics-based modelling of fission gas swelling and release in  $\text{uo}_2$  applied to integral fuel rod analysis. *Nuclear Engineering and Design*, 256:75–86, 2013.

45. Giovanni Pastore, LP Swiler, Jason D Hales, Stephen R Novascone, Danielle M Perez, Benjamin W Spencer, Lelio Luzzi, P Van Uffelen, and Richard L Williamson. Uncertainty and sensitivity analysis of fission gas behavior in engineering-scale fuel modeling. *Journal of Nuclear Materials*, 456:398–408, 2015.
46. Masaomi Oguma. Microstructure effects on fracture strength of uo2 fuel pellets. *Journal of Nuclear Science and Technology*, 19(12):1005–1014, 1982.
47. K Shrestha, T Yao, J Lian, D Antonio, M Sessim, MR Tonks, and Krzysztof Gofryk. The grain-size effect on thermal conductivity of uranium dioxide. *Journal of Applied Physics*, 126(12):125116, 2019.
48. L Bourgeois, Ph Dehaudt, C Lemaignan, and J. P Fredric. Pore migration in UO2 and grain growth kinetics. *Journal of Nuclear Materials*, 295(1):73–82, May 2001.
49. O. V. Khoruzhii, S. Yu. Kourtchatov, and V. V. Likhanskii. New model of equiaxed grain growth in irradiated UO2. *Journal of Nuclear Materials*, 265(1):112–116, February 1999.
50. Håkan Hallberg and Yaochan Zhu. Stability of grain boundary texture during isothermal grain growth in UO2 considering anisotropic grain boundary properties. *Journal of Nuclear Materials*, 465:664–673, October 2015.
51. Michael R. Tonks, Yongfeng Zhang, Xianming Bai, and Paul C. Millett. Demonstrating the Temperature Gradient Impact on Grain Growth in UO2 Using the Phase Field Method. *Materials Research Letters*, 2(1):23–28, January 2014.
52. Karim Ahmed, Janne Pakarinen, Todd Allen, and Anter El-Azab. Phase field simulation of grain growth in porous uranium dioxide. *Journal of Nuclear Materials*, 446(1–3):90–99, March 2014.
53. Michael R. Tonks, Yongfeng Zhang, Aaron Butterfield, and Xian-Ming Bai. Development of a grain boundary pinning model that considers particle size distribution using the phase field method. *Modelling Simul. Mater. Sci. Eng.*, 23(4):045009, April 2015.
54. Karim Ahmed, Michael Tonks, Yongfeng Zhang, Bulent Biner, and Anter El-Azab. Particle-grain boundary interactions: A phase field study. *Computational Materials Science*, 134:25–37, June 2017.
55. Yaolin Guo, Zhen Liu, Qing Huang, Cheng-Te Lin, and Shiyu Du. Abnormal grain growth of UO2 with pores in the final stage of sintering: A phase field study. *Computational Materials Science*, 145:24–34, April 2018.
56. Mohamed N Rahaman. *Ceramic processing and sintering*. CRC press, 2003.
57. C. E. Krill III and L. Q. Chen. Computer simulation of 3-D grain growth using a phase-field model. *Acta Materialia*, 50(12):3059–3075, July 2002.
58. Qiang Yu and Sven K. Esche. Three-dimensional grain growth modeling with a Monte Carlo algorithm. *Materials Letters*, 57(30):4622–4626, December 2003.
59. Hsun Hu and B. B. Rath. On the time exponent in isothermal grain growth. *MT*, 1(11):3181–3184, November 1970.

60. Paul Van Uffelen, Rudy JM Konings, Carlo Vitanza, and James Tulenko. Analysis of reactor fuel rod behavior. *Handbook of nuclear engineering*, pages 1519–1627, 2010.
61. C. B. Basak, A. K. Sengupta, and H. S. Kamath. Classical molecular dynamics simulation of UO<sub>2</sub> to predict thermophysical properties. *Journal of Alloys and Compounds*, 360(1):210–216, October 2003.
62. Gunter Gottstein, Lasar S. Shvindlerman, and Lasar S. Shvindlerman. *Grain Boundary Migration in Metals : Thermodynamics, Kinetics, Applications, Second Edition*. CRC Press, December 2009.
63. Michael R. Tonks, Yongfeng Zhang, S. B. Biner, Paul C. Millett, and Xianming Bai. Guidance to design grain boundary mobility experiments with molecular dynamics and phase-field modeling. *Acta Materialia*, 61(4):1373–1382, February 2013.
64. J.D. Powers and A.M. Glaeser. Grain Boundary Migration in Ceramics. *Interface Science*, 6(1):23–39, February 1998.
65. Amani Cheniour, Michael R Tonks, Bowen Gong, Tiankai Yao, Lingfeng He, Jason M Harp, Benjamin Beeler, Yongfeng Zhang, and Jie Lian. Development of a grain growth model for u3si2 using experimental data, phase field simulation and molecular dynamics. *Journal of Nuclear Materials*, page 152069, 2020.
66. Xian-Ming Bai, Yongfeng Zhang, and Michael R. Tonks. Testing thermal gradient driving force for grain boundary migration using molecular dynamics simulations. *Acta Materialia*, 85:95–106, February 2015.
67. Hao Sun and Chuang Deng. Direct quantification of solute effects on grain boundary motion by atomistic simulations. *Computational materials science*, 93:137–143, 2014.
68. A. C. S. Sabioni, W. B. Ferraz, and F. Millot. Effect of grain-boundaries on uranium and oxygen diffusion in polycrystalline UO<sub>2</sub>. *Journal of Nuclear Materials*, 278(2):364–369, April 2000.
69. Yixiong Liu and B. R. Patterson. Stereological analysis of Zener pinning. *Acta Materialia*, 44(11):4327–4335, November 1996.
70. AR Eivani, S Valipour, H Ahmed, J Zhou, and J Duszczuk. Effect of the size distribution of nanoscale dispersed particles on the zener drag pressure. *Metallurgical and Materials Transactions A*, 42(4):1109–1116, 2011.
71. Kunok Chang, Weiming Feng, and Long-Qing Chen. Effect of second-phase particle morphology on grain growth kinetics. *Acta Materialia*, 57(17):5229–5236, 2009.
72. Suk-Joong L Kang and Yang-Il Jung. Sintering kinetics at final stage sintering: model calculation and map construction. *Acta materialia*, 52(15):4573–4578, 2004.
73. Richard L Williamson, JD Hales, SR Novascone, MR Tonks, DR Gaston, CJ Permann, D Andrs, and RC Martineau. Multidimensional multiphysics simulation of nuclear fuel behavior. *Journal of Nuclear Materials*, 423(1-3):149–163, 2012.
74. Michael R Tonks, David Andersson, Simon R Phillpot, Yongfeng Zhang, Richard Williamson, Christopher R Stanek, Blas P Uberuaga, and Steven L Hayes. Mechanistic materials modeling for nuclear fuel performance. *Annals of nuclear energy*, 105:11–24, 2017.

75. IAEA. Improvement of Computer Codes Used for Fuel Behaviour Simulation (FUMEX-III): Report of a Coordinated Research Project 2008-2012. Technical Report IAEA-TECDOC-1697, International Atomic Energy Agency, 2013.